Spectroscopic Study of Nitric Acid and Water Adsorption on Oxide Particles: Enhanced Nitric Acid Uptake Kinetics in the Presence of Adsorbed Water

A. L. Goodman,† E. T. Bernard,‡ and V. H. Grassian*,†,‡

Departments of Chemistry and Chemical and Biochemical Engineering, University of Iowa, Iowa City, Iowa 52242

Received: October 10, 2000; In Final Form: April 11, 2001

In this study, the heterogeneous reactivity of nitric acid on oxide particles of some of the most abundant crustal elements is investigated at 296 K. The oxide particles are used as models for mineral dust aerosol found in the atmosphere. Transmission FT-IR spectroscopy is used to probe changes in the spectrum of the oxide particle surface following adsorption of HNO_3 on SiO_2, α-Al_2O_3, TiO_2, γ-Fe_2O_3, CaO, and MgO. It is found that HNO_3 molecularly and reversibly adsorbs on SiO_2. For the other oxides investigated, HNO_3 dissociatively and irreversibly adsorbs to form surface nitrate. There is also a small amount of molecularly adsorbed nitric acid (<10% of the adsorbed nitrate) on the oxide particle surface in the presence of gas-phase nitric acid. Because adsorbed water may play a role in the heterogeneous uptake of nitric acid in the atmosphere, transmission FT-IR spectroscopy is used to investigate H_2O adsorption on SiO_2, α-Al_2O_3, TiO_2, γ-Fe_2O_3, CaO, and MgO particles as well. Uptake of water on the oxide particles can be described by a multilayer adsorption isotherm. Water uptake on nitrate-coated oxides remained similar for α-Al_2O_3 and TiO_2 compared to the uncoated surface; however, for γ-Fe_2O_3, CaO, and MgO, the shape of the adsorption isotherm changed for the nitrate-coated particles with an increased amount of water adsorption at a given relative humidity. The infrared spectrum of the surface nitrate shows that water adsorbed on the particle surface can solvate the nitrate ion. The rate of nitric acid uptake on α-Al_2O_3 and CaO is found to increase by nearly 50-fold when going from conditions near 0 to 20% relative humidity, indicating that the nitric acid dissociation kinetics on the wetted particle surface is significantly enhanced. In the case of MgO and CaO, the amount of nitric acid uptake is increased in the presence of water and is not limited to the surface of the particles, producing saturated solutions of $Mg(NO_3)_2$ and $Ca(NO_3)_2$. From the studies presented here, atmospheric implications of heterogeneous reactions of HNO_3 with mineral dust aerosol are discussed.

Introduction

Ozone concentrations in the troposphere are highly affected by NO_x (=NO_2 + NO) and HNO_3 concentrations, the main nitrogen oxide reservoir species, because ozone is formed by a complex series of photochemical reactions involving nonlinear interactions with NO_x.[1,2] Current atmospheric chemistry models have trouble reconciling the relative concentrations of HNO_3 and NO_x and tend to overestimate the HNO_3 to NO_x ratio by a factor of 5−10,[3−5] especially in the spring and summer seasons when dust storms in Asia are prevalent.[6] Recent kinetic measurements for the OH + NO_2 indicate that this rate has been overestimated,[7] and thus the model and field measurements are in somewhat better agreement.[8] However, there is still a discrepancy which is thought to be largely due to the fact that HNO_3 concentrations are over-predicted in atmospheric chemistry models, and this discrepancy may potentially be caused by an important yet unknown chemical pathway involving the heterogeneous removal of HNO_3 from the atmosphere.[9,10] Heterogeneous processes are often neglected in most tropospheric chemistry models because there is a great amount of uncertainty in the rates of these processes.

Several studies on the heterogeneous removal of HNO_3 on cirrus clouds,[11−13] sulfate,[4] and soot[14] aerosol surfaces have been reported; however, modeling studies indicate that these processes are not significant enough to reduce the HNO_3 to NO_x ratio when included in global atmospheric chemistry models.[9,15,16] A recent modeling study by Dentener et al. has suggested that heterogeneous reactions on mineral dust aerosols may affect the NO_y (=NO_2 + NO + HNO_3), SO_x (=SO_2 + sulfate), and O_3 budgets.[17] It was found that gas-phase nitric acid may be neutralized by reacting with mineral aerosols to form particulate nitrate.[1]

Mineral aerosols are produced from wind-blown soils and represent an important component of the earth's atmosphere. It is currently estimated that between 1000 and 3000 Tg of mineral aerosols are emitted annually into the atmosphere.[18,19] Tegen and Fung estimate that 50% of tropospheric dust originates from disturbed soils.[20] The world's major regions that contribute to mineral-aerosol emissions extends from North Africa's wet coast across the Arabian Peninsula to central Asia.[21] In addition, mineral-aerosol emissions may increase substantially as arid regions expand because of changes in land use, mining, and industrial activities.[22] For the most part, atmospheric scientists have been mostly concerned with the optical properties of mineral aerosols and the role they play in climate forcing through radiative cooling or warming[23−25] and as cloud-condensation nuclei.[26] Recent modeling and field observations suggest that mineral aerosol could act as a reactive surface with trace atmospheric gases, thus, influencing the trace atmospheric

* To whom correspondence should be addressed.
† Department of Chemistry.
‡ Department Chemical and Biochemical Engineering.

10.1021/jp003722l CCC: $20.00
Published on Web 06/13/2001

gas budget through heterogeneous reactions.[17,27] Furthermore, studies in which aerosol-particle emissions are chemically analyzed support the prediction that HNO_3 reacts with mineral aerosol, in that mineral aerosols are coated with nitrate. Dentener et al. calculated that more than 40% of the total atmospheric nitrate is associated with mineral aerosol.[17] Hanel further investigated the properties of nitrate-coated atmospheric aerosol particles as a function of relative humidity and showed that Saharan mineral dust, once coated with sulfates and nitrates, can take up substantial amounts of water when relative humidity is above 50%.[28] Han and Martin found that ammonium nitrate particles internally mixed with oxide particles had substantially different hydroscopic behavior compared to that of the separated particles.[29] Goodman et al. showed that water uptake on $CaCO_3$ particles substantially increased after the particles were reacted with HNO_3 and that saturated solutions of $Ca(NO_3)_2$ formed on the surface of the particles surface at 20% relative humidity.[30]

As the above studies indicate, gas-phase and aerosol chemistry are linked in ways not accounting for in chemistry models. Specifically, HNO_3 concentrations appear to be connected to mineral-aerosol concentrations and aerosol water uptake. Thus, it is important to quantify and understand heterogeneous processes involving mineral aerosol. In this study, we have undertaken a comprehensive investigation of the heterogeneous reaction of HNO_3 on oxide particles of the most abundant crustal elements. Because mineral-aerosol particles are mainly composed of silica and silicate minerals, oxide particles of some of the most abundant crustal elements were chosen as model systems for mineral aerosol present in the troposphere. These model systems are chemically much simpler than mineral aerosol found in the atmosphere but are used to provide some insight into adsorption mechanisms and the fate of adsorbed species in heterogeneous atmospheric chemistry. Transmission FT-IR spectroscopy is used to investigate the adsorption of HNO_3 and H_2O on oxide particles: SiO_2, α-Al_2O_3, TiO_2, γ-Fe_2O_3, CaO, and MgO. The adsorption data have been analyzed and modeled to quantify the coverage of surface adsorbed water in terms of adsorbed water layers and the saturation coverage of adsorbed nitric acid in molecules cm^{-2}. In addition, transmission FT-IR spectroscopy was used to measure the kinetics of HNO_3 adsorption on oxide particles in the presence and absence of water. The HNO_3 and H_2O adsorption data is used to explain the enhanced reaction kinetics measured for nitric acid uptake in the presence of water vapor. Possible atmospheric implications of these results are discussed.

Experimental Section

The following oxide particles were used in the study: SiO_2, α-Al_2O_3, TiO_2, γ-Fe_2O_3, CaO, and MgO. Particles were characterized by their BET surface area using a Quantachrome Nova 1200 multipoint BET apparatus and by particle size using a Hitachi H-6000 transmission electron microscope. The commercial source, average particle size, BET surface area, and approximate sample weight of the oxides studied are listed in Table 1.

For FT-IR measurements, the oxide particles were prepared by either pressing or spraying an oxide/water slurry onto half of a tungsten grid (Buckbee Mears, 100 lines per inch tungsten mesh wire widths of 0.0015 in. and thickness of 0.002 in.). The other half of the grid was left blank for gas-phase measurements. The grid half coated with the oxide powder was placed inside the infrared cell. The infrared cell used in this study is modified from the design used in previous studies.[31] The modified infrared cell consists of a stainless steel cube with two germanium windows and a sample holder. The inside of the stainless steel cube is coated with Teflon in order to avoid HNO_3 decomposition on the walls of the infrared cell. The oxide samples prepared on the tungsten grid are secured inside the infrared cell by Teflon coated sample holder jaws. The infrared cell is connected to a vacuum chamber through a Teflon tube and two consecutive glass gas manifolds with ports for gas introduction and two absolute pressure transducers (range 0.001−10.000 Torr and 0.1−1000.0 Torr). The total volume of the infrared cell is 2015 ± 4 mL (infrared cube 177 ± 2 mL, first glass manifold 509 ± 1 mL, and second glass manifold 1329 ± 1 mL). The vacuum chamber consists of a two stage pumping system, a turbomolecular/mechanical pump for pumping to 10^{-7} Torr, and a mechanical pump for rough pumping to 10^{-3} Torr.

TABLE 1: Characterization of Oxide Particles: Commercial Source, Average Particle Size, BET Surface Area, and Typical Sample Weights Used in These Experiments

oxide sample	commercial source	average particle size (nm)	surface area (m^2/g)	typical sample weights (mg)
SiO_2	Degussa	20	230	28
α-Al_2O_3	Alfa Aesar	1000	14	26
TiO_2	Degussa	25	50	20
γ-Fe_2O_3	Alfa Aesar	110	50	43
CaO	Alfa Aesar	1300	4	12
MgO	Alfa Aesar	1000	15	9

The infrared cell is mounted on a linear translator inside the FT-IR spectrometer. The translator allows both halves of the grid, the blank side for gas phase measurements and the oxide coated side for surface measurements, to be probed by simply moving the infrared cell through the IR beam path. Infrared spectra were recorded with a single beam Mattson RS-10000 spectrometer equipped with a narrow band MCT detector. Typically, 250 scans were collected with an instrument resolution of 4 cm^{-1} in the spectral range extending from 4000 to 750 cm^{-1}. Some of the oxides are opaque in the lower spectral range, e.g., SiO_2 is opaque below ~1250 cm^{-1} and α-Al_2O_3 is opaque below ~900 cm^{-1}. Absorbance spectra for gas and adsorbed species were obtained by referencing single beam spectra of the blank grid and the oxide coated grid to single beam spectra collected prior to gas exposure.

Dry gaseous nitric acid was taken from the vapor of a 1:3 mixture of concentrated HNO_3 (70.6% HNO_3, Mallinckrodt) and 95.9% H_2SO_4, (Mallinckrodt). Distilled H_2O (Milli-Q) was degassed prior to use.

Results

Classification of Oxide Particles. Oxide particles are often classified according to their Lewis and Bronsted sites.[32] However, Lewis and Bronsted sites are often closely linked, and in some cases, adsorption of water may generate both types of sites. One approach is to consider the net acidic or basic behavior of the oxide, where the tendency of the anion to donate electrons is compared to the tendency of the cation to accept electrons. Tanaka and Tamaru observed a relation between the partial charge on the oxygen and the acidity of dissolved oxides and applied their findings in determining the acidity of solid oxides.[33] The partial charge on the oxygen is related directly to the electronegativity of the cation; therefore, increased cation electronegativity results in a more acidic oxide.[34] Tanaka and Tamaru suggest that the acidity of the oxide is a function of the cation radius, the anion radius, and the formal charge.[33]

Filimov et al., using the net acidity theory, related the acidity of a series of oxides to the electronegativity of the cation and found the acidity of some of the oxides of interest here to be ordered as follows: $Al_2O_3 > TiO_2 > MgO$.[35]

Another method of distinguishing the type and strength of acid centers on oxide particles is by the infrared absorptions of adsorbed pyridine.[36] Infrared absorptions of adsorbed pyridine provides information about Bronsted and Lewis acid sites. Shibata et al. have showed some correlation between acidity determined by pyridine absorption and acidity determined by cation electronegativity.[37] The results from infrared studies of pyridine adsorption show MgO as a basic oxide, Al_2O_3 as an acidic oxide, and SiO_2 as a neutral oxide.[38] Although, it is important to recognize that many of the acidic oxides are actually amphoteric and have basic sites as well.

In this study, we classify the oxides into the following three groups by applying the electronegativity theory and pyridine infrared adsorption predictions as neutral (SiO_2), amphoteric (α-Al_2O_3, TiO_2, and γ-Fe_2O_3), and basic (CaO and MgO). As will be shown, we can further classify the oxides into the above three groups according to their reactivity with HNO_3 in the presence of H_2O as nonreactive neutral insoluble (SiO_2), reactive insoluble (α-Al_2O_3, TiO_2, and γ-Fe_2O_3), and reactive basic soluble (CaO and MgO). As will be discussed, nonreactive and reactive respectively refers to whether HNO_3 weakly adsorbs on the oxide particle or whether HNO_3 can react and dissociate on the oxide surface to form adsorbed nitrate ion. The classes insoluble and soluble for the mineral oxides were determined from bulk measurements, where the oxide powders were placed into beakers and then first immersed in H_2O followed by the addition of HNO_3. Upon addition of water, none of the oxides dissolved to any great extent. However, when HNO_3 was added to a water suspension containing either CaO or MgO particles, it was found that these basic oxides instantly dissolved, whereas the other oxides did not. This is important as it will be shown that the reactivity of HNO_3 with CaO and MgO is not limited to the surface of these particles in the presence of water vapor and that a saturated solution of $M(NO_3)_2$, where M = Mg or Ca, forms on the particle surface in the presence of adsorbed water.

Water Adsorption on Oxide Particles. First, the FT-IR spectra following the adsorption of H_2O on oxide particles, SiO_2, α-Al_2O_3, TiO_2, γ-Fe_2O_3, CaO, and MgO, at 296 K as a function of pressure will be discussed. The spectra of water adsorbed on the surface of the oxides particles at water vapor pressures between 0.43 and 20.3 Torr, corresponding to 2−96% relative humidity, are shown in Figure 1. The assignment of the vibrational bands of water adsorbed on these particles is given in Table 2.[39] In these experiments, oxide particles were loaded in the infrared cell and evacuated to 10^{-7} Torr overnight. FT-IR spectra collected of SiO_2, α-Al_2O_3, and TiO_2 particles showed absorptions associated with hydroxyl groups on the surface of the oxide particles prior to exposure to water vapor.[40] FT-IR spectra collected of γ-Fe_2O_3, CaO, and MgO particles prior to water adsorption revealed surface carbonate bands between 1492 and 1429 cm^{-1} (CO_3^{2-} ν_3 asymmetric stretch[40]). Heating oxide samples under vacuum can remove surface adsorbed carbonate by forming gas-phase CO_2. Difference spectra of the oxide particles, γ-Fe_2O_3, CaO, and MgO, where spectra collected before heating were subtracted from spectra collected after heating, showed negative absorption bands between 1437 and 1480 cm^{-1}, indicating loss of surface carbonate.[41]

Following pretreatment of the oxide particles (i.e., evacuation overnight or evacuation/heating), a known pressure of water vapor was admitted into the infrared cell containing the oxide particles. When the pressure of the gas reached equilibrium, two spectra were recorded: one of the gas phase and the other of the surface in the presence of the gas. Absorbance spectra of only the adsorbed species were obtained by referencing an oxide sample spectrum after water absorption to an oxide spectrum prior to reaction. This gave a spectrum that showed absorptions of water adsorbed on the oxide surface and absorptions due to gas-phase water. Gas-phase absorption bands measured through the blank grid could then be subtracted from the spectrum in order to obtain a spectrum of surface species only. Sharp and noisy features in the regions between 3800 and 2600 cm^{-1} and 1830 and 1460 cm^{-1} in Figure 1 are residual gas-phase water absorptions left over after the subtraction procedure.[42]

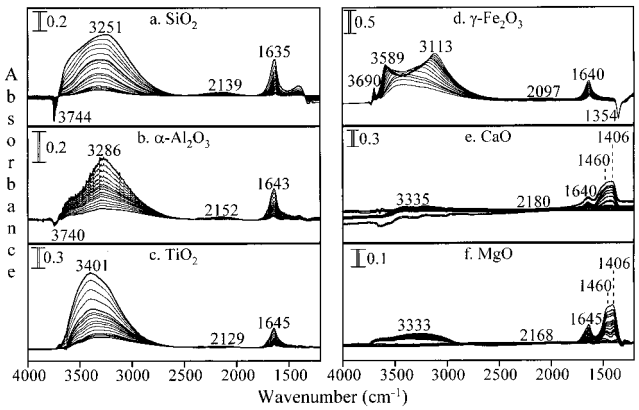

Figure 1. a−f: Transmission FT-IR spectra of water adsorption on a. SiO_2, b. α-Al_2O_3, c. TiO_2, d. γ-Fe_2O_3, e. CaO, and f. MgO particles at 296 K as a function of pressure between 2 and 96% relative humidity corresponding to water pressures of 0.430 to 20.3 Torr. FT-IR spectra of adsorbed water were recorded in the presence of the water vapor. Each spectrum was referenced to the appropriate clean oxide spectrum prior to exposure to water vapor. Gas-phase absorptions were then subtracted from each spectrum.

TABLE 2: Assignment of Vibrational Bands of H_2O Adsorbed on SiO_2, α-Al_2O_3, TiO_2, γ-Fe_2O_3, CaO, and MgO

vibrational mode	SiO_2[a]	α-Al_2O_3	TiO_2	γ-Fe_2O_3	CaO	MgO
O−H stretching	3251	3286	3401	3589[b] 3113	3335	3333
H−O−H bending	1635	1643	1645	1640	1640	1645
association[c]	2139	2152	2129	2097	2180	2168

[a] Frequencies in cm^{-1}. [b] The O−H stretching region was broad with two absorption peaks centered at 3589 and 3113 cm^{-1}. [c] The association mode (ν_a) is a combination of the bending, liberation, and hindered translation modes $\nu_2 + \nu_L - \nu_T$, respectively.[39] It is a weak broad band observed in each spectrum.

Water adsorption on SiO_2 particles as a function of increasing water vapor pressure between 2 and 96% relative humidity is shown in Figure 1a. The broad O−H stretching absorption band ranges from 3800 to 2600 cm^{-1} and is centered at 3251 cm^{-1}. A negative band at 3744 cm^{-1} due to a decrease in the intensity of the isolated O−H groups terminated on the SiO_2 particles shows that water molecules adsorbing on the SiO_2 surface are interacting with these O−H groups. The H−O−H bending mode is centered at 1635 cm^{-1}. A weaker band centered at 2139 cm^{-1} is assigned to a combination band.

Infrared spectra collected for water uptake on α-Al_2O_3, TiO_2, and γ-Fe_2O_3 (Figure 1b−d) between 2 and 96% relative humidity were similar to spectra obtained for water on SiO_2 particles (Figure 1a). The O−H stretching and H_2O bending adsorption bands centered respectively at ∼3390 and at ∼1640 cm^{-1} for α-Al_2O_3 and TiO_2 compare well to the band centers

obtained for water absorption on SiO_2 at 3251 and 1635 cm^{-1}. In the case for γ-Fe_2O_3, the H_2O bending absorption band compares well to the other oxides, but as higher relative humidity is reached, the O−H stretching band for γ-Fe_2O_3 shows different spectral characteristics in that the absorption band splits into two bands with centers at 3589 and 3113 cm^{-1}. Ishikawa et al. have studied FT-IR adsorption spectra of ferric oxide hydroxides and found γ-[Fe(O)OH] to have a strong absorption band at 3160 cm^{-1} and two weak absorption bands at 3624 and 3328 cm^{-1}.[43] The O−H stretching band split that we observe for water uptake on γ-Fe_2O_3 is most visible at high relative humidity and may indicate that γ-Fe_2O_3 is reacting with gas-phase water to form surface γ-[Fe(O)OH].

Water adsorption on heat-treated CaO and MgO particles was then studied as a function of increasing vapor pressure between 2 and 96% RH (Figure 1e,f). Adsorption bands due to surface adsorbed water at ∼3390 and ∼1640 cm^{-1} were fairly weak. The H_2O bending absorption band centered at 1645 cm^{-1} for MgO and 1640 cm^{-1} for CaO is of the same shape as the other spectra collected. In addition, positive bands at 1460 and 1406 cm^{-1}, assigned to water-solvated surface carbonate, increase in intensity as the relative humidity increases.

Surface Coverage of Adsorbed Water on Oxide Particles. When water from the vapor phase condenses onto an inert surface, the gas-phase asymmetric and symmetric stretching modes at 3756 and 3657 cm^{-1}, respectively, collapse into a broad, irregularly shaped band with a maximum near 3400 cm^{-1} and full width at half-height of ∼400 cm^{-1} in the infrared spectrum. This band is primarily associated with O−H symmetric and asymmetric stretching modes with some contribution of the overtone of H_2O bending mode.[44−46] The oscillator strength of the O−H stretching motion is enhanced by 1 order of magnitude in the liquid and solid phase from that of the gas phase because of the formation of hydrogen bonds.[46] The band center for the O−H region of condensed water shifts to lower wavenumbers as higher relative humidity is reached. This is because as the water coverage increases the hydrogen-bonding arrangement of water molecules change.[47] In addition, isolated and associated hydroxyl groups terminated on the oxide particles also contribute to this region of the spectrum and their intensities and frequencies change dramatically when gas-phase water adsorbs on the surface and hydrogen bond to the terminated O−H groups already on the oxide surface.

Although the O−H region is the most thoroughly studied spectral region of liquid water, overlapping frequencies of the asymmetric and symmetric O−H stretching modes and the H_2O bending mode overtone along with the contribution of the hydroxyl groups terminated on the oxide particle surface make this region difficult to analyze when quantifying the coverage of surface adsorbed water. In comparison, the spectral region of the H_2O bending mode contains only one vibration. When water from the vapor phase condenses onto a surface, the H_2O bending mode at 1595 cm^{-1} of water vapor forms a relatively sharp, well-defined band centered near 1645 cm^{-1}.[44−46] The measured frequencies of the bending mode for water adsorbed on oxide particles, SiO_2, α-Al_2O_3, TiO_2, γ-Fe_2O_3, CaO, and MgO (Figure 1a-f), are within 10 cm^{-1} of the bending mode of water condensed on an inert surface at 1645 cm^{-1} suggesting that this vibration in both frequency and intensity is less affected by intermolecular interactions. As demonstrated in Figure 1a−f, the H_2O bending mode band shape is uniform on a variety of surfaces, whereas the shape of the surface O−H stretching band depends to a much greater extent on the detailed nature of the chemical and physical surface properties. Therefore, using the integrated absorbance of the H_2O bending absorption band to quantify water coverage on oxide particles should introduce much less uncertainty and complexity compared to the O−H stretching region.

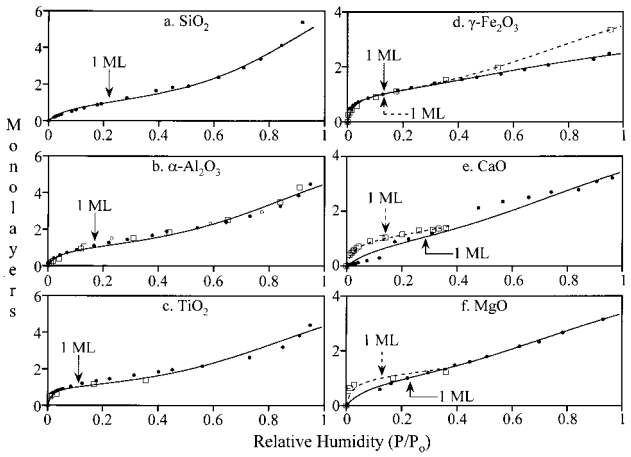

Figure 2. a−f: Water uptake on oxide particles a. SiO_2, b. α-Al_2O_3, c. TiO_2, d. γ-Fe_2O_3, e. CaO, and f. MgO particles at 296 K as a function of increasing relative humidity. The integrated area of the water-bending mode near 1640 cm^{-1} was determined as a function of relative humidity. The integrated absorbance was then converted to the number of adsorbed water layers (see text for further details). The filled circles represent experimental data for water uptake on oxide particles not reacted with HNO_3. The solid lines represent the BET fit of the experimental data according to eq 3. The open circles for α-Al_2O_3 were measured as a function of decreasing water vapor to show there is no hysteresis in the adsorption/desorption of water on this oxide. The open squares represent experimental data for water uptake on nitrate-coated oxide particles i.e., oxide particles after reaction with nitric acid. In cases where there were differences in the observed isotherm (γ-Fe_2O_3, CaO, and MgO), the dashed lines represent the BET fit of the experimental data for the nitrate-coated oxide. One monolayer of adsorbed water on each of the oxide particles is indicated by an arrow.

The coverage of adsorbed water on oxide particles, SiO_2, α-Al_2O_3, TiO_2, γ-Fe_2O_3, CaO, and MgO, can be quantified by generating adsorption isotherm curves. The bending mode absorption band of surface adsorbed water is integrated and, as discussed in detail below, integrated absorbance is converted to the number of adsorbed water layers and plotted against relative humidity, P/P_0 (Figure 2a−f, filled circles). The number of adsorbed water layers is assumed to be a linear function of the integrated absorbance of the bending mode. The data, represented by filled circles, exhibit the shape of a type II or s-shaped adsorption isotherm curve, which indicates that multilayer adsorption is occurring. The data were therefore modeled using a BET analysis.[48,49]

If adsorption takes place on an uniform surface and an infinite number of layers ($n = \infty$) build up on the surface at the saturation vapor pressure of the adsorbing gas, then most type II adsorption isotherms can be fit to the two-parameter BET eq 1

$$V = \frac{V_m c \frac{P}{P_0}}{\left(1 - \frac{P}{P_0}\right)\left(1 - \frac{P}{P_0} + c\frac{P}{P_0}\right)} \quad (1)$$

where V is the volume of gas adsorbed at equilibrium pressure P, V_m is volume of gas necessary to cover the surface of the adsorbent with a complete monolayer, P is the equilibrium pressure of the adsorbing gas, and P_0 is saturation vapor pressure of the adsorbing gas at that temperature. The parameter c is the

temperature-dependent constant related to the enthalpies of adsorption of the first and higher layers through eq 2

$$c = \exp -\left[\frac{\Delta H_1^\circ - \Delta H_2^\circ}{RT}\right] \quad (2)$$

where ΔH_1° is the standard enthalpy of adsorption of the first layer, ΔH_2° is the standard enthalpy of adsorption on subsequent layers and is taken as the standard enthalpy of condensation, R is the gas constant, and T is the temperature in Kelvin.

In most cases, the two-parameter BET equation shown above does not fit the experimental data at the highest pressures when the adsorption isotherm rises indefinitely and an infinite number of layers ($n = \infty$) of adsorbing gas is predicted to build up on the surface. A three-parameter BET eq 3 limits the number of layers of gas adsorbing at high values of P/P_0. The three-parameter BET equation is then

$$V = \left[\frac{V_m c\left(\frac{P}{P_0}\right)}{1-\left(\frac{P}{P_0}\right)}\right]\left[\frac{1-(n+1)\left(\frac{P}{P_0}\right)^n + n\left(\frac{P}{P_0}\right)^{n+1}}{1+(c-1)\left(\frac{P}{P_0}\right) - c\left(\frac{P}{P_0}\right)^{n+1}}\right] \quad (3)$$

where P, P_0, V, V_m, and c are defined as they were in eqs 1 and 2 and n is an adjustable parameter given as the maximum number of layers of the adsorbing gas and is related to the pore size and properties of the adsorbent. As a result, multilayer formation of adsorbing gas is limited to n layers at large values of P/P_0. Equation 3 models experimental data well when a finite number of layers are observed for adsorption of gases on a porous surface.

The three-parameter BET equation was used to obtain a fit to the experimental data. The parameters n, V_m, and c can be calculated according to the method discussed in detail by Joyner et al., in which eq 3 is rearranged into the linear form, shown in eq 4[50]

$$\frac{\Phi(n,x)}{V} = \frac{1}{V_m C} + \frac{\theta(n,x)}{V_m} \quad (4)$$

where

$$\Phi(n,x) = \frac{X[(1-X^n) - nX^n(1-X)]}{(1-X)^2} \quad (4a)$$

$$\theta(n,x) = \frac{X(1-X^n)}{1-X} \quad (4b)$$

and

$$X = P/P_0 \quad (4c)$$

Plots of $\Phi(n,x)/V$ with respect to $\theta(n,x)$ are made while changing the value of n until the best straight line through the experimental data points is determined. The constants V_m and c are then calculated from the slope and intercept of the straight line.

In this study, the coverage of adsorbed water on oxide particles, SiO_2, α-Al_2O_3, TiO_2, γ-Fe_2O_3, CaO, and MgO, was quantified in terms of the number of adsorbed water layers in the following way. Because the infrared data were analyzed in terms of the integrated absorbance of the bending mode, V_m is replaced by I_m, units of integrated absorbance, in the above equations and V is replaced by I, the integrated absorbance of the H_2O bending absorption mode of surface adsorbed water.

TABLE 3: Adsorption Parameters for Water Uptake on Oxide Particles SiO_2, α-Al_2O_3, TiO_2, γ-Fe_2O_3, CaO, and MgO

oxide	% RH for 1 ML[a]	n	c[b]	ΔH_1°[c]	P/P_0[d]
SiO_2	22	10	13.1	−50.3	0.021−0.84 (0.99944)
α-Al_2O_3	17	8	25.2	−52.0	0.006−0.95 (0.99683)
TiO_2	11	8	74.8	−54.6	0.019−0.95 (0.99589)
γ-Fe_2O_3	13	4	51.1	−53.7	0.009−0.95 (0.99945)
γ-Fe_2O_3*[e]	13	6	55.3	−53.9	0.004−0.95 (0.99999)
CaO	27	6	8.1	−49.2	0.011−0.96 (0.99416)
CaO*[e]	14	4	58.4	−54.0	0.012−0.36 (0.99951)
MgO	23	6	12.3	−50.2	0.12−0.93 (0.99985)
MgO*[e]	13	3	50.0	−53.6	0.006−0.36 (0.99995)

[a] Percent relative humidity corresponding to a coverage of one monolayer of adsorbed water on the oxide particles. [b] c is defined in eq 2. [c] Standard enthalpy of adsorption (kJ/mol) of H_2O on the oxide particles calculated using eq 2. [d] Range of relative humidity used for linear plots, where $P_0 = 21.08$ Torr; typically, only the central portion of the data is used for linear curve fitting. The linear correlation coefficient R is given in parentheses. [e] The asterisk indicates nitrated-oxide particles.

The integrated absorbance for one monolayer, I_m, is determined from plots of $\Phi(n,x)/I$ with respect to $\theta(n,x)$, in the same way that V_m is determined. The number of adsorbed water layers at any value of P/P_0 is just the integrated absorbance at that pressure divided by I_m (i.e., number of water layers $= I/I_m$). Using this analysis, the number of adsorbed water layers (I/I_m) versus relative humidity (P/P_0) is shown as the line through the data in Figure 2 for the oxides investigated in this study. The relative humidity, corresponding to one monolayer of water adsorbed on the oxide surfaces, is marked in Figure 2a−f for each of the oxides and is tabulated in Table 3 along with the values of n, c, and ΔH_1°. From this analysis, the following number of water layers is determined to be on the surface of these oxides as follows: approximately one monolayer at 20% relative humidity, two to three adsorbed water layers at 50% relative humidity, and three to four adsorbed water layers at 85% relative humidity, depending on the oxide surface. Our coverage estimates agree with studies of water adsorption versus relative humidity on α-Al_2O_3 powder, which show that, under typical atmospheric conditions (298 K and 50−60% relative humidity), about three monolayers of water are adsorbed on alumina surfaces.[51]

The standard enthalpy of adsorption of water vapor on the oxide surfaces, ΔH_1, was calculated from the c parameter in eq 2. The ΔH_1 values, tabulated in Table 2, range between −49.2 and −54.6 kJ/mol and are greater than the standard enthalpy of condensation of water vapor, $H_2O(g) \rightarrow H_2O(l)$, $\Delta H_2 = -44.0$ kJ/mol.

The water adsorption isotherms on oxide particles shown in Figure 2 were also investigated as a function of decreasing relative humidity for α-Al_2O_3 (Figure 2b). Filled circles represent data when water vapor was added to the infrared cell containing the oxide particles with increasing relative humidity. Open circles represent data when the water vapor pressure has been evacuated and lowered. Because the number of water layers decrease when the water vapor pressure is lowered (as indicated

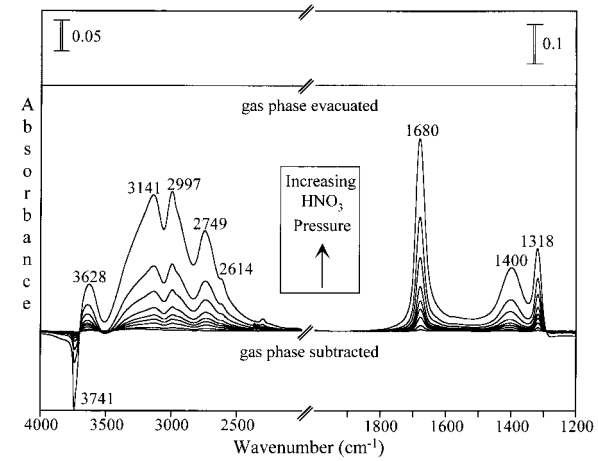

Figure 3. Transmission FT-IR spectra of HNO_3 adsorption on SiO_2 between 1200 and 4000 cm^{-1}. The phrase "gas phase subtracted" refers to infrared spectra collected as particles were exposed to increasing HNO_3 pressure: SiO_2 (3, 5, 7, 9, 13, 17, 32, 65, and 276 mTorr). The bottom spectra were all collected in the presence of the gas phase. As indicated above, contributions due to gas-phase absorptions have been subtracted from each of the spectra shown. The phrase "gas phase evacuated" refers to the spectrum recorded after evacuation of gas-phase HNO_3 following the final pressure of gas used in the experiment.

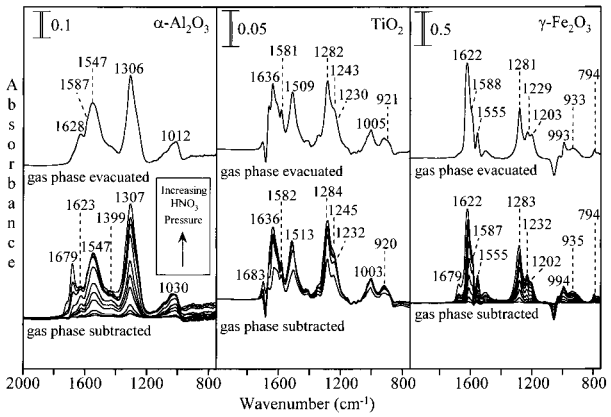

Figure 4. Transmission FT-IR spectra of HNO_3 adsorption on α-Al_2O_3, γ-Fe_2O_3, and TiO_2 between 750 and 2000 cm^{-1}. "Gas phase subtracted" refers to spectra collected as particles were exposed to increasing HNO_3 pressure for 10−15 min: α-Al_2O_3 (3, 5, 7, 9, 10, 13, 18, 28, 48, 79, 97, and 323 mTorr), γ-Fe_2O_3 (3, 5, 6, 8, 11, 14, 23, 38, 71, and 300 mTorr), and TiO_2 (6, 9, 19, 42, 85, and 329 mTorr). "Gas phase evacuated" refers to the spectrum recorded after evacuation of gas-phase HNO_3 following the final pressure of gas used in each of the experiments.

by the open circles) and follows the same path as integrated absorbance for increasing relative humidity, water adsorption on the hydroxylated-covered α-Al_2O_3 surface shows no significant hysteresis indicating reversible adsorption.

Nitric Acid Adsorption on Oxide Particles under Dry Conditions. The adsorption of nitric acid on oxide particles was initially investigated under dry conditions, i.e., in the absence of water vapor. FT-IR spectra following the reaction of HNO_3 on oxide particles, SiO_2, α-Al_2O_3, TiO_2, γ-Fe_2O_3, CaO, and MgO, at 296 K as a function of HNO_3 exposure by increasing the pressure from 3 to 300 mTorr for a period of 10−15 min are shown in Figures 3−5. The assignments of the vibrational bands of nitric acid adsorbed on these particles are given in Table 4.

The nitric acid experiments were done in a somewhat similar way to the water uptake experiments on oxide particles in that the oxide particles were loaded in the infrared cell and evacuated

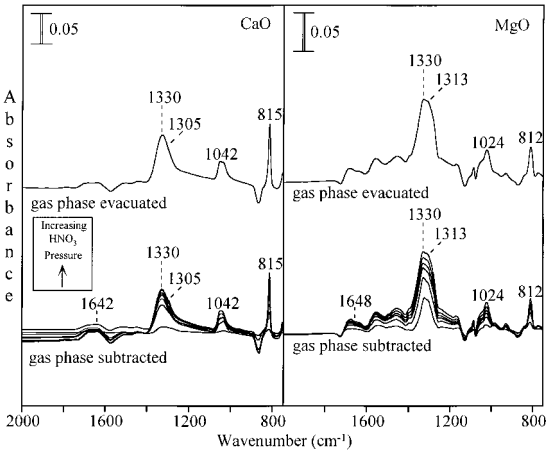

Figure 5. Transmission FT-IR spectra of HNO_3 adsorption on CaO and MgO between 750 and 2000 cm^{-1}. The phrase "gas phase subtracted" refers to spectra collected as particles were exposed to increasing HNO_3 pressure for 10−15 min: CaO (6, 11, 16, 22, 32, 51, 97, 188, 287, and 387 mTorr) and MgO (7, 13, 23, 40, 62, 82, 165, and 329 mTorr). The phrase "gas phase evacuated" refers to the spectrum recorded after evacuation of gas-phase HNO_3 following the final pressure of gas used in each of the experiments.

TABLE 4: Assignment of Vibrational Bands of Nitric Acid Adsorbed on SiO_2, α-Al_2O_3, TiO_2, γ-Fe_2O_3, CaO, and MgO

surface description	assignment	SiO_2[a]	α-Al_2O_3	TiO_2	γ-Fe_2O_3	CaO	MgO
molecularly	ν (OH)	b					
adsorbed	ν (NO_2)	1680	1679	1683	1679		
HNO_3	δ (OH)	1400	1336	1336	1337		
	ν_s (NO_2)	1318	1292	1305	1297		
ion-coordinated nitrate	ν_3 (low)					1305	1313
	ν_3 (high)					1330	1330
oxide-coordinated nitrate	monodentate						
	ν_3 (low)		1306[c]	1282	1281		
	ν_3 (high)		1547	1509	1555		
	bidentate						
	ν_3 (low)		1306[c]	1243	1229		
	ν_3 (high)		1587	1581	1588		
	bridging						
	ν_3 (low)		1306[c]	1230	1203		
	ν_3 (high)		1628	1636	1622		
	ν_1		1012	1005	993	1042	1024
	ν_2		d	d	794	815	812
adsorbed water−solvated nitrate	ν_3 (low)		1350	1331	1346	1297	1270
	ν_3 (high)		1399	1406	1399	1323	1340
	ν_1		1048	1046	1040	1046	1054
	ν_2		d	d	814	822	822

[a] Frequencies in cm^{-1}. [b] The O−H stretching region was broad (4000−2500 cm^{-1}) with absorptions at 3628, 3141, 2997, 2749, and 2614 cm^{-1}. These absorption bands shift upon deuteration to 2689, 2288, 2112, 2110, and 1900 cm^{-1}. [c] This is a broad band that is most likely composed of several bands associated with different modes of coordination to the surface. [d] Not observed below oxide lattice absorption.

to 10^{-7} Torr overnight; γ-Fe_2O_3, CaO, and MgO were not heated under vacuum. A known pressure of HNO_3 was admitted in the infrared cell containing the oxide particles for 10−15 min. Absorbance spectra of HNO_3 adsorbed on the oxide particles were obtained by referencing an oxide sample spectrum after HNO_3 was introduced into the infrared cell to an oxide background spectrum prior to HNO_3 adsorption. Gas-phase absorption bands measured through the blank grid could then be subtracted from the spectrum in order to obtain a spectrum of adsorbed HNO_3 only. Gas-phase HNO_3 was then evacuated

from the infrared cell and another spectrum was recorded and referenced to a clean oxide spectrum. The next highest pressure of HNO_3 was then admitted into the infrared cell containing the oxide. Spectra of the oxide were collected in the presence and upon evacuation of gas-phase HNO_3; this procedure was repeated again and again until the uptake began to level off as the surface became saturated.

The infrared spectra following HNO_3 adsorption on SiO_2 particles as a function of increasing HNO_3 pressure are shown in Figure 3. In the region between 2000 and 1200 cm^{-1}, three absorption bands are readily observed at 1680, 1400, and 1318 cm^{-1} and grow in intensity as the nitric acid pressure is increased from 3 to 276 mTorr (Figure 3, right panel, gas-phase subtracted). Upon evacuation of the gas phase, these three absorption bands disappear, indicating that HNO_3 desorbs from the surface upon evacuation of gas-phase nitric acid. These three bands at 1680, 1400, and 1318 cm^{-1} have been previously reported and assigned to molecularly adsorbed HNO_3: $\nu_a(NO_2)$, 1680 cm^{-1}; $\delta(OH)$, 1400 cm^{-1}; and $\nu_s(NO_2)$, 1318 cm^{-1}.[52,53] These bands are shifted by 10−68 cm^{-1} from the gas-phase HNO_3 frequencies of 1708, 1331, and 1325 cm^{-1}.[54]

In the spectral region between 2000 and 4000 cm^{-1}, there is a broad absorption band extending from 2600 to 3800 cm^{-1} that grows in intensity as the nitric acid pressure is increased from 3 to 276 mTorr (Figure 3, left panel, gas phase subtracted). At the highest HNO_3 pressures, absorption peaks at 3741, 3628, 3141, 2997, 2749, and 2614 cm^{-1} can be discerned in the broad absorption band which extends from 2600 to 3800 cm^{-1}. This complex band is assigned to the O−H stretching vibration of adsorbed HNO_3 and surface hydroxyl groups which are involved in hydrogen interactions. It is likely that the absorption peaks at 3741, 3628, 3141, 2997, 2749, and 2614 cm^{-1}, which are most evident at the highest HNO_3 pressures, arise from specific hydrogen bonding interaction between adsorbed HNO_3 and O−H groups found on the SiO_2 particles.

The fact that the molecular absorption bands of HNO_3 adsorbed on SiO_2 are not very different from gas-phase values and that HNO_3 readily desorbs from the surface upon evacuation of the gas phase shows that HNO_3 adsorption on SiO_2 is reversible at 296 K. Thus, SiO_2 is classified as a nonreactive neutral insoluble oxide in that there is no evidence for the dissociative adsorption of nitric acid on the surface of SiO_2.

The reaction of HNO_3 on α-Al_2O_3, TiO_2, and γ-Fe_2O_3 particles shows different behavior. The infrared spectra of these oxide particle surfaces as a function of increasing HNO_3 exposure are shown in Figure 4. Upon adsorption of HNO_3 on the oxide particles, several new absorption bands become evident between 750 and 2000 cm^{-1} and grow in intensity as the nitric acid pressure is increased from 3 to 300 mTorr. The absorption bands between 1200 and 1640 cm^{-1} have been reported in previous studies in our laboratory for reaction of NO_2 on oxide particles and are assigned to the degenerate ν_3 mode of oxide coordinated monodentate, bidentate and bridging nitrate which has been split into two bands because of loss of symmetry upon adsorption (see Table 4)[55,56] and have also been observed in a recent study of HNO_3 on Al_2O_3.[57] The band near 1000 cm^{-1} is assigned to the ν_1 mode of oxide coordinated nitrate. In the case for α-Al_2O_3, weak absorption bands at 1399 and 1350 cm^{-1} due to water-solvated nitrate are also apparent in the spectrum. The presence of water-solvated nitrate on oxide particles has been discussed previously.[56] As will be shown, absorption bands due to water-solvated nitrate become more apparent in the presence of gas-phase water vapor at pressures greater than 7% relative humidity.

Upon evacuation of gas-phase HNO_3, absorption bands between 750 and 2000 cm^{-1} remain in the oxide spectrum (Figure 4, gas-phase evacuated). When a difference spectrum is taken where spectra recorded upon evacuation of the gas-phase HNO_3 are subtracted from spectra recorded in the presence of gas-phase HNO_3, absorption bands at 1679, 1400, and 1318 cm^{-1} can be discerned. These absorption bands are assigned to molecularly adsorbed HNO_3. Although the absorption bands for molecularly adsorbed HNO_3 and oxide coordinated nitrate overlap, absorption bands due to molecularly adsorbed HNO_3 at ∼1680 cm^{-1} can be most readily observed in the spectra recorded at the highest nitric acid pressures. Thus, HNO_3 reacts with oxides α-Al_2O_3, TiO_2, and γ-Fe_2O_3 to primarily form oxide-coordinated nitrate, which is not removed under vacuum, and some weakly adsorbed HNO_3. Because HNO_3 reaction on α-Al_2O_3, TiO_2, and γ-Fe_2O_3 particles is mainly an irreversible process forming adsorbed nitrate ions at 296 K, we thus classify α-Al_2O_3, TiO_2, and γ-Fe_2O_3 as reactive insoluble oxides. Although the fate of the proton is difficult to unambiguously discern, the dissociated proton can react with surface hydroxyl groups to form adsorbed water or can react with surface oxygen atoms to form hydroxyl groups on the surface. It is difficult to distinguish these two mechanisms from infrared spectroscopy alone.

The adsorption of HNO_3 on CaO and MgO particles was also studied as a function of increasing HNO_3 exposure. The spectra are shown in Figure 5. In the region between 750 and 2000 cm^{-1}, four absorption bands are readily observed at 1330, 1305, 1042, and 815 cm^{-1} for CaO and 1330, 1313, 1034, and 812 cm^{-1} for MgO (Figure 5, gas-phase subtracted). These bands grow in intensity as the nitric acid pressure is increased from 6 to 387 mTorr. Upon evacuation of gas-phase HNO_3, the three absorption bands remain in the spectra (Figure 5, gas phase evacuated) without loss of intensity. This implies that the surface adsorbed species represented by bands at approximately 1330, 1042, and 815 cm^{-1} is strongly adsorbed onto the CaO and MgO particles and cannot be removed upon evacuation.

The bands at 1330, 1042, and 815 cm^{-1} for CaO and 1320, 1034, and 812 cm^{-1} for MgO are assigned to ion coordinated nitrate (ν_3 asymmetric stretch at 1330 cm^{-1}, ν_1 symmetric stretch at 1042 cm^{-1}, and ν_2 out-of-plane bend at 815 cm^{-1}) and compare well to adsorption frequencies for solid nitrate ion salts such as $Ca(NO_3)_2$(s) (ν_3 asymmetric stretch between 1358 and 1450 cm^{-1}, ν_1 symmetric stretch at 1050 cm^{-1}, and ν_2 out-of-plane bend at 822 cm^{-1}).[58] Thus, implying that, as HNO_3 reacts with CaO and MgO, nitrate is not simply forming on the oxide surface as in the case for the reactive-insoluble oxides but is reacting by a neutralization process that can be thought of as an ion exchange in which lattice oxygen atoms are replaced with nitrate ions. The overall reaction is shown as (5) and (6) for CaO and MgO, respectively.

$$CaO + 2HNO_3 \rightarrow Ca(NO_3)_2 + H_2O \quad (5)$$

$$MgO + 2HNO_3 \rightarrow Mg(NO_3)_2 + H_2O \quad (6)$$

The protons then react with oxygen atoms to form adsorbed water. The band near 1645 cm^{-1} can be assigned to the bending mode of adsorbed water and supports this conclusion. As discussed in the next section, there is evidence that this neutralization process occurs on the surface of the MgO or CaO particle and with bulk oxygen atoms as well. This exchange is facilitated by the presence of adsorbed water. The heterogeneous reaction to form $Ca(NO_3)_2$ most likely involves a two step mechanism: $MO + HNO_3 \rightarrow M(OH)NO_3 + HNO_3 \rightarrow M(NO_3)_2$

TABLE 5: Saturation Coverages for Nitric Acid Uptake on Oxide Particles SiO_2, α-Al_2O_3, TiO_2, γ-Fe_2O_3, CaO, and MgO

oxide	N_s[a]	oxide	N_s[a]
SiO_2	$7 \pm 3 \times 10^{13}$	γ-Fe_2O_3	$3 \pm 2 \times 10^{14}$
α-Al_2O_3	$6 \pm 3 \times 10^{14}$	CaO	$4 \pm 2 \times 10^{15}$
α-Al_2O_3[b]	$4 \pm 2 \times 10^{14}$	MgO	$2 \pm 1 \times 10^{15}$
TiO_2	$3 \pm 3 \times 10^{14}$	MgO[b]	$7 \pm 3 \times 10^{15}$

[a] N_s nitric acid (molecules/cm^2) corresponding to saturation coverage under dry conditions. [b] N_s nitric acid (molecules/cm^2) corresponding to saturation coverage under wet conditions.

+ H_2O(a,g), where M is Ca or Mg. Because the reaction of nitric oxide with both CaO and MgO yields oxide-ion-coordinated nitrate, CaO and MgO are classified as reactive basic soluble oxides.

Another process that contributes to the reactivity of the basic oxides involves surface carbonate that is difficult to remove upon evacuation. As shown below, in this process, gaseous CO_2 as well as water forms as a product in the reaction. There is evidence in the infrared spectrum of the formation of gas-phase CO_2 providing proof of the occurrence of the overall reactions (7)[30,59] and (8) for $CaCO_3$ and $MgCO_3$, respectively.

$$CaCO_3 + 2HNO_3 \rightarrow Ca(NO_3)_2 + CO_2 + H_2O \quad (7)$$

$$MgCO_3 + 2HNO_3 \rightarrow Mg(NO_3)_2 + CO_2 + H_2O \quad (8)$$

With the exception of SiO_2, the adsorption of HNO_3 is found to be mostly irreversible on the oxide particles investigated. In the case of the reactive oxides, HNO_3 reacts with these oxides to primarily form oxide coordinated nitrate and some weakly adsorbed nitrate. The data indicate that HNO_3 adsorption on α-Al_2O_3, TiO_2, and γ-Fe_2O_3 is about 90% irreversible at 296 K. For the reactive basic soluble oxides, HNO_3 adsorbs on these oxides to form ion-coordinated nitrate. The reaction of HNO_3 on CaO and MgO is shown to be greater than 99% irreversible.

Surface Coverage of Adsorbed Nitric Acid on Oxide Particles. To quantify nitric acid coverages, volumetric measurements were done by measuring the pressure drop in the FT-IR cell upon expansion of nitric acid from a known volume into a second known volume in the presence and absence of the oxide sample. The number of molecules of HNO_3 adsorbed on the oxide sample was determined by subtracting the number of molecules of HNO_3 adsorbed on the oxide sample and the walls of the gas handling system from the number of molecules of HNO_3 adsorbed on the walls of the gas handling system. The coverage of HNO_3 was determined by accounting for the total number of molecules adsorbed, the oxide sample weight, and the BET surface area of the oxide.

These calculated coverages are given in Table 5. The coverages obtained in this way have a fairly high level of uncertainty because volumetric measurements are difficult when the gas has some affinity for the walls of the reactor as is the case for nitric acid and the Teflon walls of the infrared cell.[60,61] The uncertainty based on duplicate measurements is approximately ±50%.

The values obtained show that SiO_2 has the lowest nitric acid coverage, $<1 \times 10^{14}$ molecules/cm^2; α-Al_2O_3, TiO_2, γ-Fe_2O_3 are all in the range of $(3-6) \times 10^{14}$ molecules/cm^2 and greater than 10^{15} molecules/cm^2, for CaO and MgO. For CaO and MgO, the coverages are greater than the expected surface coverage for a single layer. These high values are interpreted in terms of an ion displacement reaction that occurs both on the surface and a few layers into the bulk of the material. As will be shown, this process of bulk reaction is enhanced in the presence of water vapor.

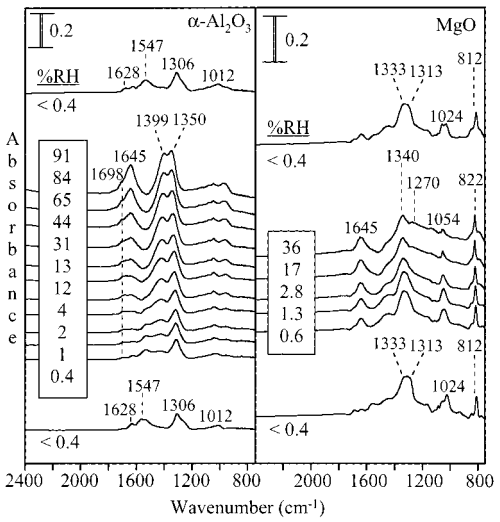

Figure 6. FT-IR spectra of water uptake on α-Al_2O_3 (left panel) and MgO (right panel) particles previously reacted with HNO_3. The spectra show conversion of surface nitrate to water-solvated nitrate with increasing relative humidity.

Water Adsorption on Oxide Particles Coated with a Nitrate Layer. Water adsorption on oxide particles α-Al_2O_3, TiO_2, γ-Fe_2O_3, CaO, and MgO saturated with HNO_3 were also investigated by FT-IR spectroscopy. Changes in the spectrum of the nitrate ion in the presence of water and changes in the uptake of water when the nitrate ion was adsorbed on the oxide particle were investigated in these experiments. The oxide particles were then exposed to HNO_3 vapor at relatively high pressure, ~300 mTorr, for thirty minutes such that the surface is saturated. The gas-phase HNO_3 was then evacuated leaving oxide coordinated nitrate ion on the α-Al_2O_3, TiO_2, and γ-Fe_2O_3, particle surface and ion coordinated nitrate on CaO and MgO particles. Water was then adsorbed on the nitrate-coated particles as a function of pressure between 2 and 96% relative humidity (0.430−20.3 Torr) at 296 K.

Water adsorption on nitrated reactive insoluble oxides (α-Al_2O_3, TiO_2, and γ-Fe_2O_3) and reactive basic soluble (MgO and CaO) oxides showed interesting behavior. Because the same spectral characteristics were observed for oxide particles in each of the two different classes, α-Al_2O_3 was chosen as a representative oxide behavior for the reactive insoluble oxides and MgO was chosen as representative oxide behavior for the reactive basic soluble oxides investigated. Representative spectra for water adsorption on nitrate-coated α-Al_2O_3 particles are shown in the left panel of Figure 6. Upon addition of water vapor to nitrated α-Al_2O_3 particles, the infrared spectra show that absorption bands assigned to oxide coordinated nitrate decrease in intensity and bands at 1645, 1399, and 1350 cm^{-1} increase in intensity. As previously discussed, the bands at 1399 and 1350 cm^{-1} correspond to solvated nitrate. The band at 1645 cm^{-1} corresponds to surface adsorbed water as observed in Figure 1. The water coverage is estimated to be around three layers for the spectra labeled 65% RH and near one monolayer for the spectra labeled 12% RH. Upon evacuation of water vapor, water-solvated nitrate converts back to oxide-coordinated nitrate (top spectrum, left panel of Figure 6). Another feature that appears in the spectrum upon the addition of water to the surface is a band near 1698 cm^{-1}. This band may be due to an associated nitric acid species in the water layer as has been observed for concentrated nitric acid solutions.[61]

Spectra of water adsorbed as a function of pressure on MgO particles that had been reacted with HNO_3 to form ion-coordinated nitrate are shown in the right panel of Figure 6. Upon addition of water vapor between 0.6 and 36% relative humidity, to nitrated MgO, the infrared spectra show that adsorption bands assigned to ion coordinated nitrate at 1330, 1313, 1025, and 813 cm^{-1} shift to higher frequency as higher relative humidity is reached. These bands shift to 1340, 1270, 1054, and 822 cm^{-1} are assigned to water-solvated nitrate. Upon evacuation of water vapor, water-solvated ion-coordinated nitrate converts back to ion-coordinated nitrate (top spectrum, right panel, Figure 6). Relative humidity greater than 36% was not investigated because loss of nitrate from the sample was found indicating a thin film of a saturated $Mg(NO_3)_2$ solution form that can fall off of the sample holder and deposit in the infrared cell chamber. A similar phenomenon was observed in studies of water uptake on nitrated calcium oxide.

The coverage of adsorbed water on nitrate-covered α-Al_2O_3, TiO_2, γ-Fe_2O_3, CaO, and MgO was quantified using the integrated absorbance of the water bending mode to determine if the water adsorption on the oxide surface was affected by the presence of the adsorbed nitrate layer. A plot of the integrated absorbance versus water pressure again generated type II adsorption isotherm curves. These data are plotted in Figure 2b−f as open squares. As demonstrated in Figure 2, the water isotherm curve for water adsorption on oxide particles of α-Al_2O_3 and TiO_2 previously reacted with HNO_3 (open squares) follows the same isotherm curve found previously for α-Al_2O_3 and TiO_2 that were not reacted with HNO_3 (filled circles, solid lines). This implies that oxide-coordinated nitrate plays no role in the net adsorption of water on these particles.

However, when the adsorption isotherm for water uptake on γ-Fe_2O_3, CaO, and MgO particles previously reacted with HNO_3 (Figure 2d−f, dashed lines, open squares) is compared to the adsorption isotherm for water uptake on particles not reacted with HNO_3 (Figure 2d−f, solid lines, filled circles), different adsorption isotherms are observed. It is apparent from the shape of the isotherm curves that water uptake on CaO and MgO is greater on reacted oxides (Figure 2e−f, dashed lines) than on oxides not reacted with HNO_3 (Figure 2e−f, solid lines) between 0 and 36% RH. The relative humidity corresponding to one monolayer of surface adsorbed water is even lower (~13% RH) for nitrated CaO and MgO compared to that of the unreacted oxides (~25% RH). As mentioned previously, the FT-IR spectra indicate that saturated solutions of $Ca(NO_3)_2$ and $Mg(NO_3)_2$ form above 36% relative humidity. In addition, the bulk measurements resulted in the complete dissolution of the CaO and MgO oxide particles when mixed with liquid water and nitric acid. Thus, this implies that the dashed line isotherm for CaO and MgO does not rise to infinity at relative humidity greater than 36% because the outer layers of the particles undergo deliquescence at the higher percent RH. The nitrated γ-Fe_2O_3 shows different behavior in that the water adsorption isotherm deviates for the nitrated particles only at the higher relative humidity.

Heterogeneous Reaction Kinetics: Uptake of Nitric Acid on SiO_2, α-Al_2O_3, and CaO. The rate of HNO_3 uptake on oxide particles was determined by time course experiments. Kinetic experiments were done on three different oxides SiO_2, α-Al_2O_3, and CaO, because they represent oxides of the three defined classes of oxides, nonreactive neutral insoluble (SiO_2), reactive insoluble (α-Al_2O_3), and reactive basic soluble (CaO). In these experiments, oxide particles, either SiO_2, α-Al_2O_3, or CaO, were loaded into the infrared cell and evacuated to 10^{-7} Torr for 3 h. A known pressure of HNO_3 vapor was then admitted into the infrared cell while infrared spectra of the oxide particles were collected every few seconds at an instrument resolution of 4 cm^{-1}.

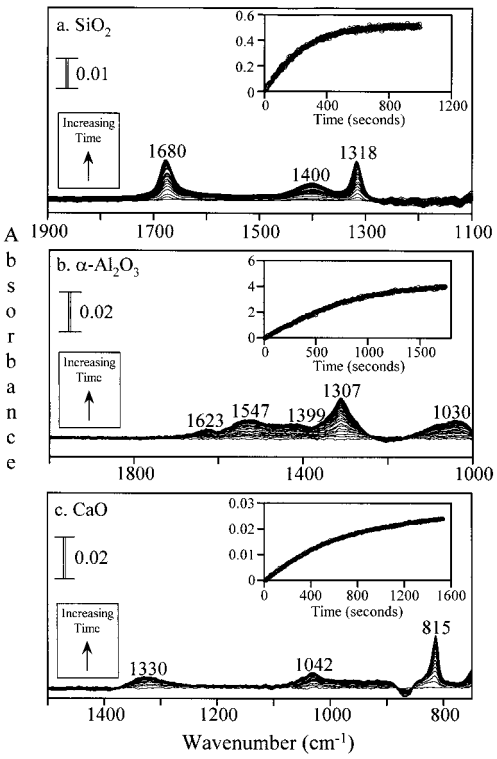

Figure 7. a−c: Transmission FT-IR spectra of HNO_3 uptake on (a) SiO_2, (b) α-Al_2O_3, and (c) CaO particles as a function of time. For clarity, only every tenth spectrum collected is shown in the main portion of the figure. The integrated absorbance (or peak height) for the absorption bands of adsorbed nitric acid is plotted as a function of time in the inset. Every spectrum collected is used for the plots in the inset.

Representative spectra collected for HNO_3 uptake on SiO_2, α-Al_2O_3, and CaO as a function of time are shown in Figure 7. In Figure 7a, SiO_2 particles were exposed to 10 mTorr of HNO_3 vapor (corresponding to 3.3×10^{14} molecules/cm^3). In this experiment, FT-IR spectra were recorded every 2.5 s (four scans per spectrum) at an instrument resolution of 4 cm^{-1} for 1000 total seconds. Nitric acid uptake on SiO_2 particles was determined by integrating the absorption band at 1680 cm^{-1}, during the course of the experiment. The integrated absorbance plotted versus time is shown in the inset of Figure 7a. Similar experimental data are shown for α-Al_2O_3 and CaO (Figure 7b,c). For α-Al_2O_3 and CaO particles, the particles were exposed to 9 mTorr corresponding to 2.9×10^{14} molecules/cm^3 and spectra were recorded every 7 s (four scans per spectrum) at an instrument resolution of 4 cm^{-1}. The extent of nitric acid uptake on α-Al_2O_3 was determined by integrating the entire region extending from 1189 to 1822 cm^{-1}. A plot of the integrated absorbance as a function of time is shown in the inset of Figure 7b. The region extending from 1189 to 1822 cm^{-1} corresponds to absorption of predominantly oxide-coordinated nitrate as well as a small amount of molecularly adsorbed HNO_3. For CaO, the peak height of the absorption band at 815 cm^{-1}, corresponding to the out-of-plane bend of the ion coordinated nitrate ion, was measured because this was found to be the best method for determining the extent of nitrate adsorption on CaO. The peak height is plotted versus time in the inset shown in Figure 7c.

TABLE 6: Kinetic Analysis—Nitric Acid Uptake on SiO_2

HNO_3 (mTorr)	HNO_3 (molecules cm^{-3})	RH[a]	rate[b] (integrated absorbance s^{-1})	rate[c] (molecules s^{-1} cm^{-2})	flux[d] (molecules s^{-1} cm^{-2})	γ[e]
7	2.3×10^{14}	0	6.8×10^{-4}	1.9×10^{9}	1.8×10^{18}	1.1×10^{-9}
8	2.6×10^{14}	0	1.0×10^{-3}	2.8×10^{9}	2.1×10^{18}	1.4×10^{-9}
9	2.9×10^{14}	0	4.7×10^{-4}	1.3×10^{9}	2.3×10^{18}	5.9×10^{-10}
9	2.9×10^{14}	0	1.3×10^{-3}	3.7×10^{9}	2.3×10^{18}	1.6×10^{-9}
10	3.3×10^{14}	0	1.6×10^{-3}	4.3×10^{9}	2.6×10^{18}	1.7×10^{-9}
11	3.6×10^{14}	0	1.1×10^{-3}	3.0×10^{9}	2.8×10^{18}	1.1×10^{-9}
11	3.6×10^{14}	0	1.6×10^{-3}	4.4×10^{9}	2.8×10^{18}	1.6×10^{-9}
12	3.9×10^{14}	0	1.8×10^{-3}	4.9×10^{9}	3.1×10^{18}	1.6×10^{-9}
13	4.2×10^{14}	0	2.0×10^{-3}	5.4×10^{9}	3.3×10^{18}	1.6×10^{-9}
14	4.6×10^{14}	0	2.3×10^{-3}	6.3×10^{9}	3.6×10^{18}	1.8×10^{-9}
15	4.9×10^{14}	0	2.4×10^{-3}	6.9×10^{9}	3.9×10^{18}	1.8×10^{-9}
16	5.2×10^{14}	0	2.6×10^{-3}	7.2×10^{9}	4.1×10^{18}	1.7×10^{-9}
17	5.5×10^{14}	0	3.1×10^{-3}	8.5×10^{9}	4.4×10^{18}	1.9×10^{-9}
19	6.2×10^{14}	0	3.5×10^{-3}	9.7×10^{9}	4.9×10^{18}	2.0×10^{-9}

[a] Percent relative humidity. [b] Rate measured in integrated absorbance s^{-1}. [c] Rate converted to molecules cm^{-2} s^{-1}. [d] Flux of HNO_3. [e] Calculated uptake coefficient.

For heterogeneous reactions, the uptake of a gas on a solid is most often expressed in terms of an uptake coefficient or reaction probability, γ. Equation 9 defines γ as the rate of adsorption divided by rate of gas−surface collisions

$$\gamma = \frac{(dN_a/dt)}{\text{Flux}} \tag{9}$$

where the numerator is the rate of formation of surface-bound species on the oxide particles upon reaction with HNO_3 vapor (units of molecules/cm^2 s) and the denominator is the flux or collision rate per unit area of HNO_3 vapor with the oxide particles (units of molecules/cm^2 s). The flux is calculated according to the kinetic gas theory

$$\text{Flux} = \frac{PN}{(2\pi MRT)^{1/2}} \tag{10}$$

where P is the pressure of HNO_3, N is Avogadro's number, M in the molecular weight of the gas, R is the gas constant, and T is the temperature. The rate of formation of surface-bound species on the oxide particles upon reaction with HNO_3 vapor can be described by the rate law

$$dN_a/dt = k(1 - \theta)N_s P \tag{11}$$

where dN_a/dt is the rate of formation of surface-bound species on the oxide particles upon reaction with HNO_3 vapor, k is the rate constant of adsorption, $(1 - \theta)$ is the number of sites on the oxide particles available for reaction and $\theta = N_a/N_s$, N_s is the saturation coverage on the oxide particles, and P is the pressure of HNO_3 vapor. As discussed for the heterogeneous uptake of NO_2 on NaCl[62,63] and Al_2O_3,[57] if the pressure, P, is constant and the number of sites on the oxide particles, $(1 - \theta)$, is large compared to the number of surface-bound species formed, θ, then the rate of formation of surface-bound species on the oxide particles, dN_a/dt, is proportional to the slope of a plot of N_a versus time.

By making the above assumptions of constant pressure and a large number of surface sites, we have determined the uptake coefficient for HNO_3 on SiO_2, α-Al_2O_3, and CaO. The rate of adsorption on the oxide particles, the numerator of eq 9, was calculated from the slope of the peak height or integrated absorbance of surface-bound species versus time. The inset of Figure 7a−c depicts this type of plot for SiO_2, α-Al_2O_3, and CaO. The following rates were calculated from the initial linear portion of the integrated absorbance (or peak height) versus time plots for the data presented in Figure 7. These rates were determined in units of integrated absorbance (or peak height) per second and then converted to molecules/cm^2 s^{-1} using the calibration determined in the last section. The flux, the denominator of eq 9, was calculated from eq 10. Tables 6−8 summarize the data used to calculate γ. The average uptake coefficient for HNO_3 is determined to be $(1.6 \pm 0.3) \times 10^{-9}$, $(4 \pm 1) \times 10^{-8}$, and $(4 \pm 1) \times 10^{-7}$ on SiO_2, α-Al_2O_3, and CaO, respectively, under dry conditions. The uptake coefficient was found to have slight pressure dependence for nitric acid uptake on SiO_2 and no pressure dependence for nitric acid uptake on α-Al_2O_3 and CaO.

The main assumptions in the above analysis are that the HNO_3 pressure is constant, the number of sites on the oxide particles is uniform and large, and $1 - \theta$ is close to 1, i.e., the fraction of sites covered, θ, is small. The error associated with these assumptions is small for HNO_3 uptake on SiO_2 particles: ∼2% error in assuming pressure is constant and ∼2% error in assuming $1 - \theta$ is equal to 1. In the case of α-Al_2O_3 and CaO, the error associated with these assumptions is higher for HNO_3 uptake: as large as 15% error assuming pressure is constant and 12% error in assuming $1 - \theta$ is equal to 1. Thus, there is an error of 25−30% associated with the uptake coefficient calculated for α-Al_2O_3 and CaO on dry surfaces under the assumption of a uniform site distribution. Another underlying assumption is that diffusion into the layers is facile and rapid. Problems associated with these assumptions are given in the Discussion section.

The rate of HNO_3 uptake on α-Al_2O_3 and CaO particles was also investigated in the presence of adsorbed water which was varied by doing experiments at different percent RH. The same experimental procedure described above was followed except that the oxide particles in the infrared cell were exposed to mixtures of HNO_3 and H_2O vapor. For the experiments with water vapor present, it was necessary to increase the HNO_3 concentration as some of the gas-phase HNO_3 was lost in the water layer on the reaction vessel walls. The increased uptake on the walls was determined in separate experiments. Thus, the measured uptake is a lower limit as the flux to the surface is overestimated in the analysis of γ. The uptake of HNO_3 on α-Al_2O_3 and CaO particles in the presence of water vapor was complete somewhere between 3 and 30 s after the experiment began, which is many times faster than the uptake of HNO_3 on particles under dry conditions. Therefore, spectra were collected at the maximum data acquisition rate of 1.67 scans per second (1 scan per spectrum) at an instrument resolution of 8 cm^{-1}. At

TABLE 7: Kinetic Analysis—Nitric Acid Uptake on α-Al_2O_3

HNO_3 (mTorr)	HNO_3 (molecules cm^{-3})	RH[a]	rate[b] (integrated absorbance s^{-1})	rate[c] (molecules s^{-1} cm^{-2})	flux[d] (molecules s^{-1} cm^{-2})	γ[e]
5	1.6×10^{14}	0	1.3×10^{-3}	3.1×10^{10}	1.3×10^{18}	2.4×10^{-8}
6	2.0×10^{14}	0	1.9×10^{-3}	4.6×10^{10}	1.5×10^{18}	3.0×10^{-8}
7	2.3×10^{14}	0	3.5×10^{-3}	8.4×10^{10}	1.8×10^{18}	4.7×10^{-8}
7	2.3×10^{14}	0	3.4×10^{-3}	8.1×10^{10}	1.8×10^{18}	4.5×10^{-8}
9	2.9×10^{14}	0	4.0×10^{-3}	9.5×10^{10}	2.3×10^{18}	4.1×10^{-8}
11	3.6×10^{14}	0	3.6×10^{-3}	8.5×10^{10}	2.8×10^{18}	3.0×10^{-8}
13	4.2×10^{14}	0	6.9×10^{-3}	1.6×10^{11}	3.3×10^{18}	4.9×10^{-8}
25	8.2×10^{14}	1.6	8.0×10^{-3}	2.8×10^{11}	6.4×10^{18}	4.4×10^{-8}
38	1.2×10^{15}	1.9	7.6×10^{-2}	2.7×10^{12}	9.8×10^{18}	2.8×10^{-7}
39	1.3×10^{15}	1.9	7.9×10^{-2}	2.8×10^{12}	1.0×10^{19}	2.8×10^{-7}
40	1.3×10^{15}	2.0	1.7×10^{-1}	5.9×10^{12}	1.0×10^{19}	5.71×10^{-7}
44	1.4×10^{15}	2.2	2.0×10^{-1}	6.9×10^{12}	1.1×10^{19}	6.1×10^{-7}
51	1.7×10^{15}	3.1	2.7×10^{-1}	9.5×10^{12}	1.3×10^{19}	7.3×10^{-7}
76	2.5×10^{15}	4.7	5.6×10^{-1}	2.0×10^{13}	2.0×10^{19}	1.0×10^{-6}
101	3.3×10^{15}	6.3	1.1×10^{-1}	3.8×10^{13}	2.6×10^{19}	1.5×10^{-6}
76	2.5×10^{15}	6.3	4.8×10^{-1}	1.7×10^{13}	2.0×10^{19}	8.7×10^{-7}
83	2.7×10^{15}	9.4	6.4×10^{-1}	2.3×10^{13}	2.1×10^{19}	1.1×10^{-6}
88	2.9×10^{15}	11.0	9.7×10^{-1}	3.4×10^{13}	2.3×10^{19}	1.5×10^{-6}
152	4.9×10^{15}	13.0	1.2×10^{0}	4.2×10^{13}	3.9×10^{19}	1.1×10^{-6}
126	4.1×10^{15}	14.0	1.2×10^{0}	4.3×10^{13}	3.2×10^{19}	1.3×10^{-6}
152	4.9×10^{15}	16.0	2.0×10^{0}	7.1×10^{13}	3.9×10^{19}	1.8×10^{-6}

[a] Percent relative humidity. [b] Rate measured in integrated absorbance s^{-1}. [c] Rate converted to molecules cm^{-2} s^{-1}. [d] Flux of HNO_3. [e] Calculated uptake coefficient.

TABLE 8: Kinetic Analysis—Nitric Acid Uptake on CaO

HNO_3 (mTorr)	HNO_3 (molecules cm^{-3})	RH[a]	rate[b] (peak height s^{-1})	rate[c] (molecules s^{-1} cm^{-2})	flux[d] (molecules s^{-1} cm^{-2})	γ[e]
4	1.3×10^{14}	0	9.6×10^{-6}	3.3×10^{11}	1.0×10^{18}	3.2×10^{-7}
5	1.6×10^{14}	0	1.1×10^{-5}	3.9×10^{11}	1.3×10^{18}	3.0×10^{-7}
6	2.0×10^{14}	0	1.2×10^{-5}	4.3×10^{11}	1.5×10^{18}	2.8×10^{-7}
6	2.0×10^{14}	0	9.8×10^{-6}	3.4×10^{11}	1.5×10^{18}	2.2×10^{-7}
7	2.3×10^{14}	0	1.4×10^{-5}	4.7×10^{11}	1.8×10^{18}	2.6×10^{-7}
8	2.6×10^{14}	0	2.3×10^{-5}	8.0×10^{11}	2.1×10^{18}	3.9×10^{-7}
9	2.9×10^{14}	0	3.0×10^{-5}	1.0×10^{12}	2.3×10^{18}	4.5×10^{-7}
11	3.6×10^{14}	0	3.0×10^{-5}	1.0×10^{12}	2.8×10^{18}	3.7×10^{-7}
11	3.6×10^{14}	0	1.8×10^{-5}	6.4×10^{11}	2.8×10^{18}	2.2×10^{-7}
14	4.6×10^{14}	0	5.5×10^{-5}	1.9×10^{12}	3.6×10^{18}	5.3×10^{-7}
16	5.2×10^{14}	0	3.8×10^{-5}	1.3×10^{12}	4.1×10^{18}	3.2×10^{-7}
18	5.9×10^{14}	0	6.6×10^{-5}	2.3×10^{12}	4.6×10^{18}	5.0×10^{-7}
23	7.5×10^{14}	0	5.5×10^{-5}	1.9×10^{12}	5.9×10^{18}	3.2×10^{-7}
27	8.8×10^{14}	0	1.3×10^{-4}	4.4×10^{12}	6.9×10^{18}	6.3×10^{-7}
37	1.2×10^{14}	0	9.9×10^{-5}	3.5×10^{12}	9.5×10^{18}	3.6×10^{-7}
25	8.2×10^{14}	0.31	2.8×10^{-5}	9.6×10^{11}	6.4×10^{18}	1.5×10^{-7}
20	6.5×10^{14}	0.94	5.1×10^{-6}	1.8×10^{11}	5.1×10^{18}	3.5×10^{-8}
25	8.2×10^{14}	1.6	4.3×10^{-4}	1.5×10^{13}	6.4×10^{18}	2.3×10^{-6}
32	1.0×10^{15}	1.7	3.5×10^{-4}	1.2×10^{13}	8.2×10^{18}	1.5×10^{-6}
38	1.2×10^{15}	1.9	1.2×10^{-3}	4.2×10^{13}	9.8×10^{18}	4.3×10^{-6}
40	1.3×10^{15}	2.0	5.7×10^{-4}	2.0×10^{13}	1.0×10^{19}	1.9×10^{-6}
48	1.6×10^{15}	2.7	1.7×10^{-3}	5.7×10^{13}	1.2×10^{19}	4.7×10^{-6}
51	1.7×10^{15}	3.1	1.9×10^{-3}	6.5×10^{13}	1.3×10^{19}	4.9×10^{-6}
61	2.0×10^{15}	4.1	3.4×10^{-3}	1.2×10^{14}	1.6×10^{19}	7.5×10^{-6}
61	2.0×10^{15}	4.1	2.1×10^{-3}	7.2×10^{13}	1.6×10^{19}	4.6×10^{-6}
63	2.1×10^{15}	4.4	3.7×10^{-3}	1.3×10^{14}	1.6×10^{19}	7.9×10^{-6}
25	8.2×10^{14}	6.3	1.7×10^{-3}	5.8×10^{13}	6.4×10^{18}	8.9×10^{-6}
101	3.3×10^{15}	6.3	5.7×10^{-3}	2.0×10^{14}	2.6×10^{19}	7.6×10^{-6}
44	1.4×10^{15}	13.0	3.2×10^{-3}	1.1×10^{14}	1.1×10^{19}	9.9×10^{-6}

[a] Percent relative humidity. [b] Rate measured in absorption band peak height s^{-1}. [c] Rate converted to molecules cm^{-2} s^{-1}. [d] Flux of HNO_3. [e] Calculated uptake coefficient.

relative humidity greater than 17%, the reaction of HNO_3 on α-Al_2O_3 and CaO saturated in less than three seconds, thus, limiting our ability to measure reaction probability much above 17% relative humidity.

The uptake coefficient for the reaction of HNO_3 on α-Al_2O_3 and CaO in the presence of water vapor was calculated using eq 9. The uptake coefficient for HNO_3 on α-Al_2O_3 and CaO increased by as much as 50-fold as relative humidity increased from 0 to 16%. The increase in the uptake coefficient on the wetted surface as a function of relative humidity is shown in Figure 8. The open circles represent the enhancement in the reactive uptake coefficient, $\gamma_{wet}/\gamma_{dry}$, of HNO_3 on α-Al_2O_3 and CaO particles as a function of relative humidity. The solid line represents the BET isotherm fit for water adsorption on α-Al_2O_3 and CaO particles in which the parameter V_m, the volume of adsorbed water on the oxide particles corresponding to a coverage of one monolayer, was replaced by γ_m, the uptake coefficient measured at a water coverage of one monolayer, in

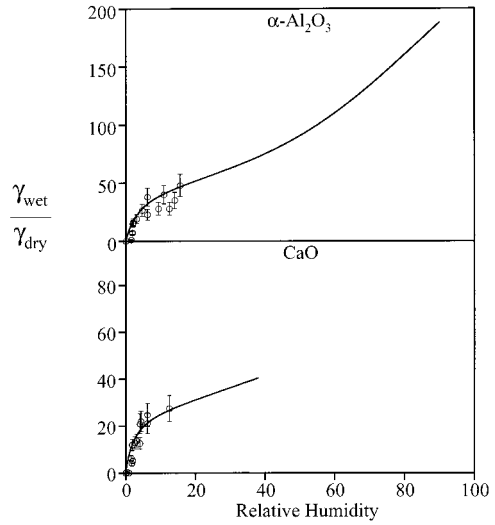

Figure 8. Enhancement of the reactive uptake as a function of relative humidity for HNO_3 uptake on α-Al_2O_3 and CaO particles. Open circles represent $\gamma_{wet/dry}$ as a function of relative humidity. The solid lines represent the modified BET isotherm fit for water adsorption on α-Al_2O_3 and CaO particles as determined previously except now calibrated to $\gamma_{m,wet}$ as shown in eq 8 and discussed in the text. For CaO, the nitrate-coated isotherm is used.

eq 3, as suggested in a recent paper by Davis and Cox for nitric acid uptake on NaCl.[64] This equation can be written as

$$\gamma_{wet} = \left(\frac{\gamma_{wet,m} c\left(\frac{P}{P_0}\right)}{1-\left(\frac{P}{P_0}\right)}\right)\left(\frac{1-(n+1)\left(\frac{P}{P_0}\right)^n + n\left(\frac{P}{P_0}\right)^{n+1}}{1+(c-1)\left(\frac{P}{P_0}\right) - c\left(\frac{P}{P_0}\right)^{n+1}}\right) \quad (12)$$

Thus, the BET parameters for the isotherm curve for water uptake on α-Al_2O_3 particles are now $\gamma_{wet,m} = 1.82 \times 10^{-6}$ at 16% RH with $c = 25.2$ and $n = 8$. In the case of CaO, the BET isotherm curve for water uptake on nitrate-covered CaO particles was used to model the γ dependence. The parameters for CaO are now $\gamma_{wet,m} = 9.90 \times 10^{-6}$ at 13% RH with $c = 39.7$ and $n = 4.1$. The ratio of $\gamma_{wet}/\gamma_{dry}$ as a function of relative humidity and the calculated $\gamma_{wet}/\gamma_{dry}$ from the water isotherm curve shows that the HNO_3 uptake rate on oxide particles is enhanced in the presence of water vapor and that this enhancement can be understood in terms of the increased adsorbed water layers on the oxide particles.

The effect of water vapor on the net uptake of HNO_3 on the oxide particles was investigated. In these experiments, the reaction of HNO_3 on α-Al_2O_3 was investigated as a function of HNO_3 pressure in the presence of water vapor corresponding to 30 ± 2% relative humidity. The ν_3 absorbance band of oxide-coordinated nitrate resulting when gas-phase HNO_3 or HNO_3 and H_2O are evacuated was integrated for spectra recorded under dry and wet conditions and plotted versus HNO_3 equilibrium pressure. The net uptake of HNO_3 for α-Al_2O_3 is slightly less under wet conditions then under dry conditions. The uptake of HNO_3 on MgO particles in the absence and presence of water vapor was also compared in the same manner as described for α-Al_2O_3. The data show that nitric acid adsorbs more in the presence of water vapor on MgO at 30 ± 2% RH as compared to uptake under dry conditions and at coverages greater than one monolayer suggesting that the bulk oxygen atoms participate in the reaction as well as the surface oxygen atoms and that this participation is enhanced in the presence of water vapor similar to what has been observed for the heterogeneous uptake of HNO_3 on $CaCO_3$ particles as shown in our previous study.[30]

Discussion

Water Adsorption on Oxide Particles Under Ambient Conditions, T = 296 K and 0−90% RH. A molecular level understanding of water adsorption on solid substrates is a topic of great interest. There has been an enormous amount of insight gained in this regard for water adsorption on salt crystals from the work of Ewing and co-workers and their studies of water adsorption on NaCl(100) surfaces.[47,65−67] Single-crystal surfaces are ideal substrates for gaining insight into the molecular level details of the adsorption process. From a large shift in the vibrational frequency of the O−H stretching mode and a jump in the integrated absorbance, it was inferred from transmission FT-IR data that at 295 K water initially adsorbs on NaCl(100) in two-dimensional islands at submonolayer coverages and then begins three-dimensional growth and multilayer adsorption between 30 and 45% RH. It was also shown that Na^+ and Cl^- ions are incorporated into the water layer at coverages above 2 ML.

There have been some recent theoretical and experimental studies of water adsorption on single-crystal oxide particles under ambient conditions that have provided a greater understanding of the oxide-water interface under ambient conditions.[68−74] Using synchrotron diffraction techniques, Eng et al. examined the structure of the hydrated α-Al_2O_3(0001) surface.[68] The fully hydrated surface is oxygen-terminated with a contracted aluminum layer underneath and is found to have a structure which is intermediate between α-Al_2O_3 and γ-$Al(OH)_3$ with a semiordered layer of adsorbed water.[68]

In this study, water adsorption on oxide particles at 296 K was characterized by transmission FT-IR spectroscopy. As discussed, the O−H stretching region is complex for oxide particle surfaces, because hydrogen-bonded hydroxyl groups and adsorbed water all contribute to the intensity of the O−H stretching region. Analysis of the bending mode of adsorbed water shows that on the oxides investigated here (SiO_2, α-Al_2O_3, TiO_2, α-Fe_2O_3, CaO, and MgO) there is no obvious discontinuity in the integrated absorbance nor is there a jump in the vibrational frequency for this mode as the water coverage increases from 0 to 96%. As discussed previously, the bending mode is not as perturbed by intermolecular interactions compared to the O−H stretching mode. Thus, the bending mode is not as useful in gaining insight into intermolecular interactions as compared to the O−H stretching mode. However, the analysis of the bending mode allows for the quantification of the number of adsorbed water layers on the particle surface as a function of relative humidity using a classical BET adsorption model. From the BET fit, monolayer coverages are defined and coverage-averaged enthalpies of adsorption can be determined. From this analysis, the following generalizations can be made. Near 20% RH, there is approximately one layer of adsorbed water on the oxide particles investigated, and the range of values goes from 11 to 27% RH. At 50% RH, water coverages above one monolayer are present, close to two layers in most cases. Near 80% RH, there are between two and four adsorbed layers, depending on the oxide.

Although useful in defining monolayer coverages and quantifying adsorbed water layers as a function of percent RH, the BET analysis provides little insight into the details of the molecular adsorption process because it does not take into account lateral adsorbate−adsorbate interactions. Clearly this is a major oversimplification for water adsorption which will form two- and three-dimensional hydrogen bonding networks. In addition, because of the heterogeneous nature of the particle surfaces, average behavior can be characterized and, therefore,

sometimes only a limited amount of insight into fundamental interactions can be gained. The BET analysis can then be used to find an empirical functional form of the water adsorption isotherm. The empirical equation can potentially be incorporated into atmospheric models and used to model uptake coefficients as a function of the atmospheric water content.

Adsorption of water on a nitrated surface may provide some insight into the molecular nature of the adsorbed water layers. The infrared data show for the reactive insoluble oxides (e.g., α-Al_2O_3) regions of oxide coordinated and water-solvated nitrate ions coexist at relative humidity below 30%, as discussed previously by Miller and Grassian.[56] This suggests that there is some islanding of the water molecules on the surface at coverages near and below one monolayer, as suggested by Ewing and co-workers.[47,65−67] Because the adsorption isotherms are similar for these oxides (α-Al_2O_3, TiO_2, and α-Fe_2O_3) in the region from 0 to 35% RH for oxide particles that have reacted with nitric acid compared to oxide particles that were not reacted, the data suggest that some islanding may be occurring as well on oxide particles that were not reacted with nitric acid. For the reactive soluble oxides, the data indicate that saturated solutions of $M(NO_3)_2$ (where $M = Mg^{2+}$ and Ca^{2+}) form, similar to what is observed for nitric acid uptake on $CaCO_3$.[30]

Nitric Acid Adsorption on Oxide Particles—Adsorption Mechanism and Reaction Kinetics. Nitric acid adsorption on SiO_2 is completely reversible:

$$HNO_3(g) \rightleftarrows HNO_3(a) \qquad (13)$$

The SiO_2 surface is terminated by hydroxyl groups, and it is reasonable to assume that the nature of the interaction between the SiO_2 surface and molecular nitric acid involves a hydrogen bonding interaction.

For the other oxides, the majority of the adsorption is irreversible in that upon evacuation of the gas-phase adsorbed products remain. The following reaction sequence is proposed for the reactive uptake of nitric acid on α-Al_2O_3, TiO_2, γ-Fe_2O_3, CaO, and MgO:

$$HNO_3(g) \rightarrow [HNO_3(a)] \rightarrow H^+(a) + NO_3^-(a) \qquad (14)$$

It is unclear whether the adsorption involves a molecular precursor state, $HNO_3(a)$, prior to the dissociation step as has been recently proposed by Davis and Cox for HNO_3 uptake on NaCl.[64]

Although the nitrate ion can be easily monitored by infrared spectroscopy, the fate of the proton is less defined. The proton may react on the surface with surface hydroxyl groups or oxygen atoms to form adsorbed water, i.e.

$$HNO_3 + M(OH) \rightarrow MNO_3(a) + H_2O(a) \qquad (15)$$

$$2HNO_3 + M'O \rightarrow M'(NO_3)_2(a) + H_2O(a) \qquad (16)$$

where M = Al, Ti, or Fe and M′ = Ca or Mg. In the presence of adsorbed water, the adsorbed water layer provides another medium for the dissociation reaction and can be written as

$$HNO_3(g) + H_2O(a) \rightarrow H_3O^+(aq) + NO_3^-(aq) \qquad (17)$$

The reaction kinetics are most likely more complex than the analysis provided here suggests. At least two mechanisms may be operative, one involving adsorbed water and the other not. Thus, the total rate of nitrate adsorption can be thought of as follows:

$$(dN_a/dt) = k_{dry}N^x_{HNO_3}(site) + k_{water}N_{HNO_3}N_{H_2O} \qquad (18)$$

where the adsorption rate is composed of two parts: one being adsorption on the dry surface in the absence of adsorbed water and the other being adsorption that involves surface adsorbed water. The kinetics of these two steps are very different. What makes the kinetics even more complex is that water appears to be forming during the course of the reaction such that the kinetics maybe changing as well. Another complication is that there may be strongly adsorbed water on the particle surface even under dry conditions suggesting that the mechanism represented by reaction 17 may be important under all conditions investigated in this study, as has been suggested by Biechert and Finlayson-Pitts and Ghosal and Hemminger in the uptake of nitric acid on NaCl particles.[75,76]

The uptake coefficients reported here are quite low, and these values may not represent accurate values of the uptake coefficient for several reasons. The most important being that diffusion of the reactants through the powder is not instantaneous but will occur on the time scale of the measurement and not all layers are accessed simultaneously. It takes a longer amount of time to access underlying layers. So, the uptake coefficient is being measured for a powdered sample which at any given time will have each layer saturated to a different extent. For example, the first layer will adsorb and saturate first and the middle layers will saturate last (molecules are colliding with the "front" and the "back" of the oxide powder pressed onto the tungsten grid; thus, the middle layers represent the least accessible layers of the powder). At the pressures used in these experiments, some layers may be saturating within the first second or two of the experiment. The effect of diffusion and saturation of some layers very quickly will be that the experimentally measured value of the uptake coefficient will be much lower, potentially by several orders of magnitude, than the initial uptake coefficient which is what is often times reported in the literature.

Atmospheric Implications. This study was done to address the question of whether HNO_3 removal by mineral dust would be significant to reduce the HNO_3 to NO_x ratio when included in global atmospheric chemistry models. The laboratory study showed that all of the oxide particles can adsorb HNO_3 and, except, for SiO_2 this can be considered as reactive uptake on these oxide particle surfaces. In addition, our studies indicate that the reaction of HNO_3 with CaO and MgO is not to be limited to the surface and can react into the bulk of each of the particles. The dependence of water on the reactive uptake is clearly demonstrated in this study in that, as relative humidity increases, γ increases by almost 50-fold and follow the water adsorption isotherm measured in this study.

The value of the reactive uptake coefficient is significantly lower than that measured in recent Knudsen cell studies even though in the Knudsen cell study, the BET area of the entire sample was used and not just the geometric area of the sample holder.[77,78] The Knudsen cell studies were done at much lower pressures on the order of a factor of 10^3 lower. Thus, saturation effects are minimized in the Knudsen cell experiments. The assumption of a uniform site distribution might not be valid, and the most reactive sites may be probed at the lower pressures. The water content of the particles is also difficult to control under dry conditions and may be different in the two experiments. In a recent box-model study[78] on α-Al_2O_3, TiO_2, and γ-Fe_2O_3, reactive uptakes greater than 10^{-6} were found to reduce

nitric acid concentrations. Although the values reported here are 10^{-5} or below, they represent lower limits because these experiments were done at pressures much higher than those present in the atmosphere. The uptake coefficient for many of the oxides studied here were determined from the Knudsen cell studies to be greater than 10^{-5} at 296 K even under dry conditions using nitric acid pressures on the order of 10 ppb. Because of the constraints of Knudsen flow, the effects of relevant water vapor pressures on the heterogeneous uptake kinetics cannot be easily explored with this technique. Thus, it is proposed that the effects due to adsorbed water found here be used in atmospheric models (e.g., using the BET analysis as a functional form of the number of adsorbed water layers) but that the kinetic data determined from Knudsen cell studies be used in the models as they were collected at much lower HNO_3 pressures more representative of that found in the atmosphere and at pressures such that saturation effects are minimized. It can then be concluded from the Knudsen cell data and the box-model study that heterogeneous reactions of HNO_3 on mineral dust should be included in atmospheric chemistry models if HNO_3 levels are to be accurately predicted.

Conclusions

In this study, the adsorption of H_2O and HNO_3 on oxide particles, SiO_2, α-Al_2O_3, γ-Fe_2O_3, TiO_2, CaO, and MgO, was investigated by FT-IR spectroscopy. HNO_3 reversibly adsorbs on SiO_2 and thus exhibits nonreactive uptake. On the other oxides studied, HNO_3 irreversibly adsorbs on α-Al_2O_3, TiO_2, and γ-Fe_2O_3 to a large extent to form oxide-coordinated nitrate and on CaO and MgO to form ion-coordinated nitrate and thus exhibits reactive uptake. Water uptake on α-Al_2O_3 and TiO_2 particles is the same for unreacted and nitrate coated particles. Net H_2O adsorption on γ-Fe_2O_3, CaO and MgO particles coated with nitrate is greater than on uncoated particles. At relative humidity greater that 36%, saturated solutions of $Ca(NO_3)_2$ and $Mg(NO_3)_2$ form. By use of a modified BET adsorption model, the coverage of H_2O on oxide particles and nitrate-coated oxide particles was quantified as a function of relative humidity. The water isotherms were used to explain the enhanced adsorption kinetics for nitric acid adsorption in the presence of gas-phase water. There are some similarities observed in the heterogeneous chemistry of nitric acid on oxide particles to sea salt, especially for the reactive soluble oxides CaO and MgO.

Acknowledgment. The authors gratefully acknowledge the National Science Foundation for support of this work (CHE-9988434).

References and Notes

(1) Seinfeld, J. H. *Atmospheric Chemistry and Physics of Air Pollution*; John Wiley and Sons: New York, 1986.

(2) Sillman, S.; Logan, J. A.; Wofsy, S. C. *J. Geophys. Res.* **1990**, *95*, 1837.

(3) Liu, S. C.; Trainer, M.; Carroll, M. A.; Hubler, G.; Montzka, D. D.; Norton, R. B.; Ridley, B. A.; Walega, J. G.; Atlas, E. L.; Heikes, B. G.; Huebert, B. J.; Warren, W. *J. Geophys. Res.* **1992**, *97*, 10463.

(4) Chatfield, R. B. *Geophys. Res. Lett.* **1994**, *21*, 2705.

(5) Hauglustain, D. A.; Ridley, B. A.; Solomon, S.; Hess, P. G.; Madronich, S. *Geophys. Res. Lett.* **1996**, *23*, 2609.

(6) Carmichael, G. R.; Zhang, Y.; Chen, L. L.; Hong, M. S.; Ueda, H. *Atmos. Environ.* **1996**, *30*, 2407.

(7) Donahue, N. M.; Dubey, M. K.; Mohrschladt, R.; Demerjian, K. L.; Anderson, J. G. *J. Geophys. Res.* **1997**, *102*, 6159.

(8) Song, C. H.; Carmichael, G. R. *J. Atmos. Chem.* In press.

(9) Singh, H. B.; Herlth, D.; Kolyer, R.; Salas, L.; Bradshaw, J. D.; Sandholm, S. J.; Davis, D. D.; Crawford, J.; Knodo, Y.; Koike, M.; Talbot, R.; Gregory, G. L.; Sachse, G. W.; Browell, E.; Blake, D. R.; Rowland, F. S.; Newell, R.; Merill, J.; Hiekes, B.; Liu, S. C.; Crutzen, P. J.; Kanakidou, M. *J. Geophys. Res.* **1996**, *101*, 1793.

(10) Thakur, A. N.; Singh, H. B.; Mariani, P.; Chen, Y.; Wang, Y.; Jacob, D. J.; Brasseur, G.; Muller, J. F.; Lawerence, M. *Atmos. Environ.* **1999**, *33*, 1403.

(11) Abbatt, J. P. D.; Beyer, K. D.; Fucaloro, A. F.; McMahon, J. R.; Wooldridge, P. J.; Zhong, R.; Molina, M. J. *J. Geophys. Res.* **1992**, *97*, 15819.

(12) Zondlo, M. A.; Barone, S. B.; Tolbert, M. A. *Geophys. Res. Lett.* **1997**, *24*, 1391.

(13) Lawrence, M. G.; Crutzen, P. J. *Tellus* **1992**, *50B*, 263.

(14) Rogaski, C. A.; Golden, D. M.; Williams, L. R. *Geophys. Res. Lett.* **1997**, *24*, 381.

(15) Tabazadeh, A.; Toon, O. B. *Geophys. Res. Lett.* **1998**, *25*, 1379.

(16) Wang, Y.; Logan, J. A.; Jacob, D. J. *J. Geophys. Res.* **1998**, *103*, 10727.

(17) Dentener, F. J.; Carmichael, G. R.; Zhang, Y.; Lelieveld, J.; Crutzen, P. J. *J. Geophys. Res.* **1996**, *101*, 22869.

(18) Jonas, P.; Charlson, R.; Rodhe, H. *Aerosols in Climate Change*; Cambridge University Press: New York, 1995.

(19) d'Almeida, G. A. *J. Geophys. Res* **1987**, *92*, 3017.

(20) Tegen, I.; Fung, I. *J. Geophys. Res.* **1995**, *100*, 18707.

(21) Prospero, J. M. *Proc. Natl. Acad. Sci. U.S.A.* **1999**, *96*, 3396.

(22) Sheehy, D. A. *Ambio* **1992**, *21*, 303.

(23) Tegen, I.; Fung, I. *J. Geophys. Res.* **1994**, *99*, 22897−22914.

(24) Li, X.; Maring, H.; Savoic, D.; Voss, K.; Prospero, J. M. *Nature* **1996**, *380*, 416.

(25) Andreae, M. O. *Nature* **1996**, *380*, 389.

(26) Charlson, R. J.; Schwartz, S. E.; Hales, J. M.; Cess, R. D.; Coakley, J. A.; Hansen, J. E.; Hoffmann, D. J. *Science* **1992**, *255*, 423.

(27) Zhang, Y.; Sunwoo, Y.; Kotamarthi, V.; Carmichael, G. R. *J. Appl. Met.* **1994**, *33*, 813.

(28) Hanel, G. *Adv. Geophys.* **1976**, *19*, 73.

(29) Han, J. H.; Martin, S. T. *J. Geophys. Res.-Atmos.* **1999**, *104*, 3543.

(30) Goodman, A. L.; Underwood, G. M.; Grassian, V. H. *J. Geophys. Res.-Atmos.* **2000**, *104*, 29053.

(31) Goodman, A. L. Ph.D. Dissertation, University of Iowa, 2000.

(32) Morrison, S. R. *The Chemical Physics of Surfaces*; Plenum Press: New York, 1990.

(33) Tanaka, K.; Tamaru, K. *Bull. Chem. Soc. Jpn.* **1964**, *37*, 862.

(34) Sanderson, R. T. *Chemical Periodicity*; Van Nostrand Reinhold: New York, 1960.

(35) Filimov, V. N.; Lopatin, Y. N.; Sukhov, D. A. *Kinet. Katal.* **1969**, *10*, 458.

(36) Parry, E. P. *J. Catal.* **1963**, *2*, 371.

(37) Shibata, K.; Kyoura, T.; Kitatawa, J.; Sumiyoshi, T.; Tanabe, K. *Bull. Chem. Soc. Jpn.* **1973**, *46*, 2985.

(38) Tanabe, K. *Solid Acids and Bases*; Academic Press: New York, 1970.

(39) Williams, D. *Nature* **1966**, *210*, 194.

(40) Little, L. H. *Infrared Spectra of Adsorbed Species*; Academic Press: London, 1966.

(41) A different infrared cell was used for the experiments in which heating was needed. The apparatus has been described previously. Driessen, M. D.; Grassian, V. H. *J. Phys. Chem.* **1995**, *99*, 16519.

(42) Weis, D. D.; Ewing, G. E. *Anal. Chem.* **1998**, *70*, 3175.

(43) Ishikawa, T.; Nitta, S.; Kondo, S. *J. Chem. Soc., Faraday Trans. 1* **1986**, *82*, 2401.

(44) Luck, W. A. P. *Structure of Water and Aqueous Solutions*; Hans Richarz Publikationsservice: Germany, 1974; p 207.

(45) Eisenberg, D.; Kauzmann W. *The Structure and Properties of Water*; Oxford University Press: New York, 1969.

(46) Pimental, G. C.; McClellan, A. L. *The Hydrogen Bond*; Freeman: San Francisco, CA, 1960.

(47) Ewing, G. E.; Peters, S. J. *J. Phys. Chem. B* **1997**, *101*, 10880.

(48) Flood, E. A. *The Solid Gas Interface*; Marcel Dekker, Inc.: New York, 1966.

(49) Gregg, S. J.; Sing, K. S. *Adsorption, Surface Area and Porosity*; Academic Press: London, 1967.

(50) Joyner, L. G.; Weinberger, E. B.; Montgomery, C. W. *J. Am. Chem. Soc.* **1945**, *67*, 2182.

(51) Yan, B.-D.; Meilink, S. L.; Warren, G. W.; Wynblatt, P. *IEEE Trans. Compon., Hybrids, and Manuf. Technol.* **1987**, *10*, 247.

(52) Goodman, A. L.; Underwood, G. M.; Grassian, V. H. *J. Phys. Chem. A* **1999**, *103*, 7217.

(53) Barney, W. S.; Finlayson-Pitts, B. J. *J. Phys. Chem. A* **2000**, *104*, 171.

(54) Shimanouchi, T. *J. Phys. Chem. Ref. Data* **1977**, *6*, 1039.

(55) Underwood, G. M.; Miller, T. M.; Grassian, V. H. *J. Phys. Chem. A* **1999**, *103*, 6184.

(56) Miller, T. M.; Grassian, V. H. *Geophys. Res. Lett.* **1998**, *25*, 3835.

(57) Borensen, C.; Kirchner, U.; Scheer, V.; Vogt, R.; Zellner, R. *J. Phys. Chem. A* **2000**, *104*, 5030.

(58) Irish, D. E.; Walrafen, G. E. *J. Chem. Phys.* **1967**, *46*, 378.
(59) Fenter, F. F.; Caloz, F.; Rossi, M. *Atmos. Environ.* **1995**, *29*, 3365.
(60) Fenter, F. F.; Caloz, F.; Rossi, M. *J. Phys. Chem.* **1994**, *98*, 9801.
(61) Leuchs, M.; Zundel, G. *J. Phys. Chem.* **1978**, *82*, 1632.
(62) Vogt, R.; Finlayson-Pitts, B. J. *J. Phys. Chem.* **1994**, *98*, 3747.
(63) Peters, J. S.; Ewing, G. E. *J. Phys. Chem.* **1996**, *100*, 14093.
(64) Davies, J. A.; Cox, R. A. *J. Phys. Chem. A* **1998**, *102*, 7631.
(65) Foster, M. C.; Ewing, G. E. *J. Chem. Phys.* **2000**, *112*, 6817.
(66) Peters, S. J.; Ewing, G. E. *Langmuir* **1997**, *13*, 6345−6348.
(67) Foster, M.; Ewing, G. E. *Surf. Sci.* **1999**, *427*−*428*, 102.
(68) Eng, P. J.; Trainor, T. P.; Brown, G. E.; Waychunas, G. A.; Newville, M.; Sutton, S. R.; Rivers, M. L. *Science* **2000**, *288*, 1029.
(69) Tikhomirov, V. A.; Jug, K. *J. Phys. Chem. B* **2000**, *104*, 7619−7622.
(70) Jones, F.; Rohl, A. L.; Farrow, J. B.; van Bronswijk, W. *Phys. Chem. Chem. Phys*. **2000**, *2*, 3209.
(71) Joseph, W.; Ranke, W.; Weiss, W. *J. Phys. Chem. B* **2000**, *104*, 3224.
(72) Gunko, V. M.; Turov, V. V. *Langmuir* **1999**, *15*, 6405.
(73) Elam, J. W.; Nelson, C. E.; Cameron, M. A.; Tolbert, M. A.; George, S. M. *J. Phys. Chem. B* **1998**, *102*, 7008.
(74) Sneh, O.; Cameron, M. A.; George, S. M. *Surf. Sci.* **1996**, *364*, 61.
(75) Beichert, P.; Finlayson-Pitts, B. J. *J. Phys. Chem.* **1996**, *100*, 15218.
(76) Ghosal, S.; Hemminger, J. C. *J. Phys. Chem. A* **1999**, *103*, 4777.
(77) Underwood, G. M.; Li, P.; Al-Abadleh, H.; Grassian, V. H. *J. Phys. Chem. A.* In press.
(78) Underwood, G. M.; Song, C. H.; Phadnis, M.; Carmichael, G. R.; Grassian, V. H. *J. Geophys. Res.-Atmos.* In press.